Chapter 21

Modeling of the Structural Behavior of Fuel Elements and Assemblies

21.1 MATERIALS INPUT FUNCTIONS

From the microcosm of point defects, dislocations, and chemical reactions, we move into the domain of structural analysis, for this is the means by which atomistic theory is used to predict the macroscopic behavior of a reactor core during operation. The preceding chapters were devoted to preparing the scientific foundations necessary for rational analysis of the irradiation comportment of the principal components of the reactor, of which we shall select the fuel pin and the fuel assembly for detailed examination.

Superficially, a reactor fuel element is a simple object; its vital parts are cylindrical pellets of a fissile oxide encased in a metal tube. The ultimate purpose of the fuel-pin analysis may be simply stated: given the geometry of the fuel element (i.e., the fuel radius, the cladding thickness, and the size of the fuel—cladding gap), the initial chemical composition and porosity of the fuel, and the power history at which the pin is to operate, to calculate the length of time that the cladding performs its primary function of separating the coolant from the fuel. A fuel element is considered to have failed when the cladding is breached. The principal cause of cladding rupture is permanent strain (plastic flow and creep) due to internal loading by fission-gas pressure or fuel—cladding mechanical interaction. The apparent simplicity of the fuel pin is deceptive. Its mechanical behavior during irradiation depends on a great number of individual phenomena, only a few of which are adequately understood theoretically. These basic processes operate simultaneously within the fuel, and there is a large degree of interconnection between each of them. Figure 21.1 summarizes the complex relations between the physical, chemical, and mechanical processes (shown in ovals in Fig. 21.1) and the observable consequences on the fuel element (shown in rectangles in Fig. 21.1). Calculations based on Fig. 21.1 are so complicated that they can be performed only by high-speed computers. These computer analyses are called *fuel-modeling codes*; they attempt to follow the evolution of the important characteristics of the fuel and cladding as functions of irradiation time, beginning with the first application of power and terminating in failure by cladding rupture.
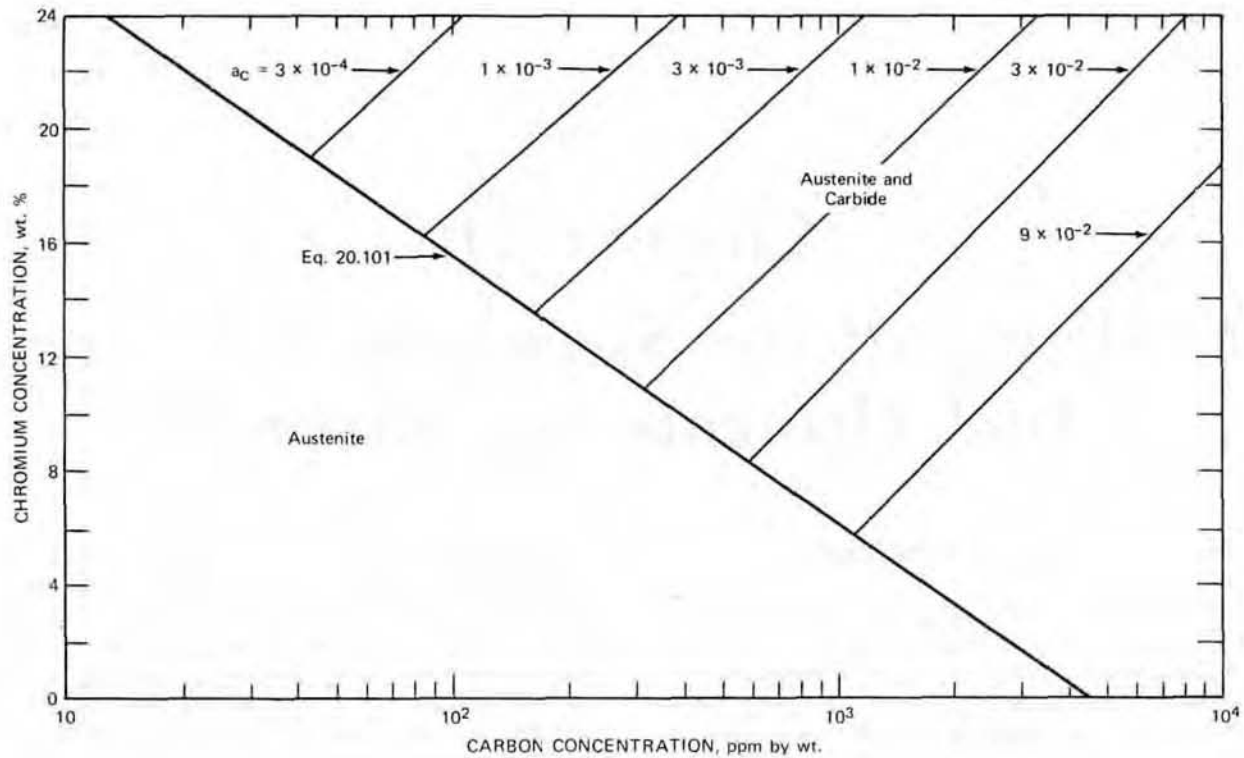
The circled items in Fig. 21.1 are the *materials input functions* for the code. These functions consist in part simply of a list of physical, chemical, or mechanical properties or they may represent calculations of the rates of particular processes (e.g., fission-gas swelling) by subroutines nearly as large as the main fuel-modeling program. The materials input functions can either be based entirely on theory or be derived from observations. Often the theoretical framework of a basic process is used with sufficient adjustable parameters to force the model to agree with observed gross changes in the fuel-pin dimensions during irradiation. This procedure is known as calibrating or fine tuning the code.

The computer programs can either be restricted to the cladding or can consider the entire fuel element. Fuel and cladding are coupled via the thermal, mechanical, and chemical links listed in the central column of Fig. 21.1. Codes that treat the entire pin are called integral fuel-modeling codes for liquid-metal fast breeder reactor (LMFBR) analysis. The most important are LIFE (U. S. National Code)[1,2] and COMETH/CRASH (Belgonucleaire).[3,4] Earlier fuel modeling codes developed in the United States[5-8] have been abandoned in favor of a concentrated development of the LIFE code. A review by Matthews[9] deals with the general problem of fuel-element modeling.

The sources of the materials input functions for the various calculations performed by the fuel-modeling code are described in the following sections.

21.1.1 Temperature Distribution
(Sec. 10.4)

Because of changes in the thermal conductivity, the porosity distribution, and the chemical distribution in the fuel during irradiation, the temperature distribution also changes slowly with time. A temperature distribution is determined at each time step by numerical solution of Eq. 10.49, using a thermal-conductivity expression that depends on fuel temperature, porosity, and oxygen-to-metal ratio and using a heat-source term that reflects the

CHROMIUM CONCENTRATION, wt. %

$a_C = 3 \times 10^{-4}$ 1×10^{-3} 3×10^{-3} 1×10^{-2} 3×10^{-2}

Austenite and Carbide

9×10^{-2}

Eq. 20.101

Austenite

CARBON CONCENTRATION, ppm by wt.

(a) Suppose that stainless steel containing 18 wt.% Cr and 8 wt.% Ni is equilibrated with sodium in which the carbon activity is 0.01. What is the total carbon content in the steel at equilibrium?

(b) What are the chromium and carbon concentrations of the austenite phase in steel that has been equilibrated with sodium having a carbon activity of 0.01?

(c) Using the chromium and carbon balances derived in the text, determine the Cr/(Cr + Fe) ratio in the carbide phase (i.e., X).

(d) What are the implications of the result of question c?

20.13 Sodium flows past a bare cylinder of mixed-oxide fuel having an initial oxygen-to-metal ratio of $2 - x_0$. The oxygen concentration in the sodium stream is C_O. The oxygen potentials of the sodium $(\Delta \overline{G_{O_2}})_{Na}$ and of the fuel $(\Delta \overline{G_{O_2}})_f$ are both lower than the threshold necessary for formation of the $Na_3 MO_4$ phase. The oxygen potential of the fresh fuel is larger than that of the sodium; thus oxygen is removed from the fuel by the flowing sodium. Equilibrium at the fuel—sodium interface is maintained, and, to permit the kinetics to be solved, we linearize Eq. 20.150 to

$$C_O = 52 - 750x \quad \text{(for } T = 1000^\circ K)$$

The oxygen dissolved from the fuel is transported into the flowing sodium by convective diffusion with a mass-transfer coefficient of k_d.

Solve the diffusion equation for the oxygen in the fuel with the appropriate conditions at the fuel—sodium interface reflecting chemical equilibrium and the transport resistance in the sodium film. How long an exposure of the fuel to sodium is required for the center line of the fuel to attain 50% of its equilibrium value?

$$D_0^f = 4 \times 10^{-13} \text{ cm}^2 /\text{sec}$$
$$R = 0.3 \text{ cm}$$
$$k_d = 0.75 \text{ cm/sec}$$
$$\rho_f / \rho_{Na} = 2$$

Hint: Use results in *Conduction of Heat in Solids* by H. Carslaw and J. C. Jaeger, *2nd* ed., Secs. 7.6 and 7.7, Oxford University Press, Inc., New York, 1959.

20.14 The maximum amount of mechanical work that can be released in the fuel—coolant interaction can be calculated thermodynamically. Suppose fuel powder at $2500^\circ K$ contacts a large body of sodium at $1000^\circ K$. What fraction of the heat content of the fuel (above $1000^\circ K$) can be converted to mechanical work in a reversible process?
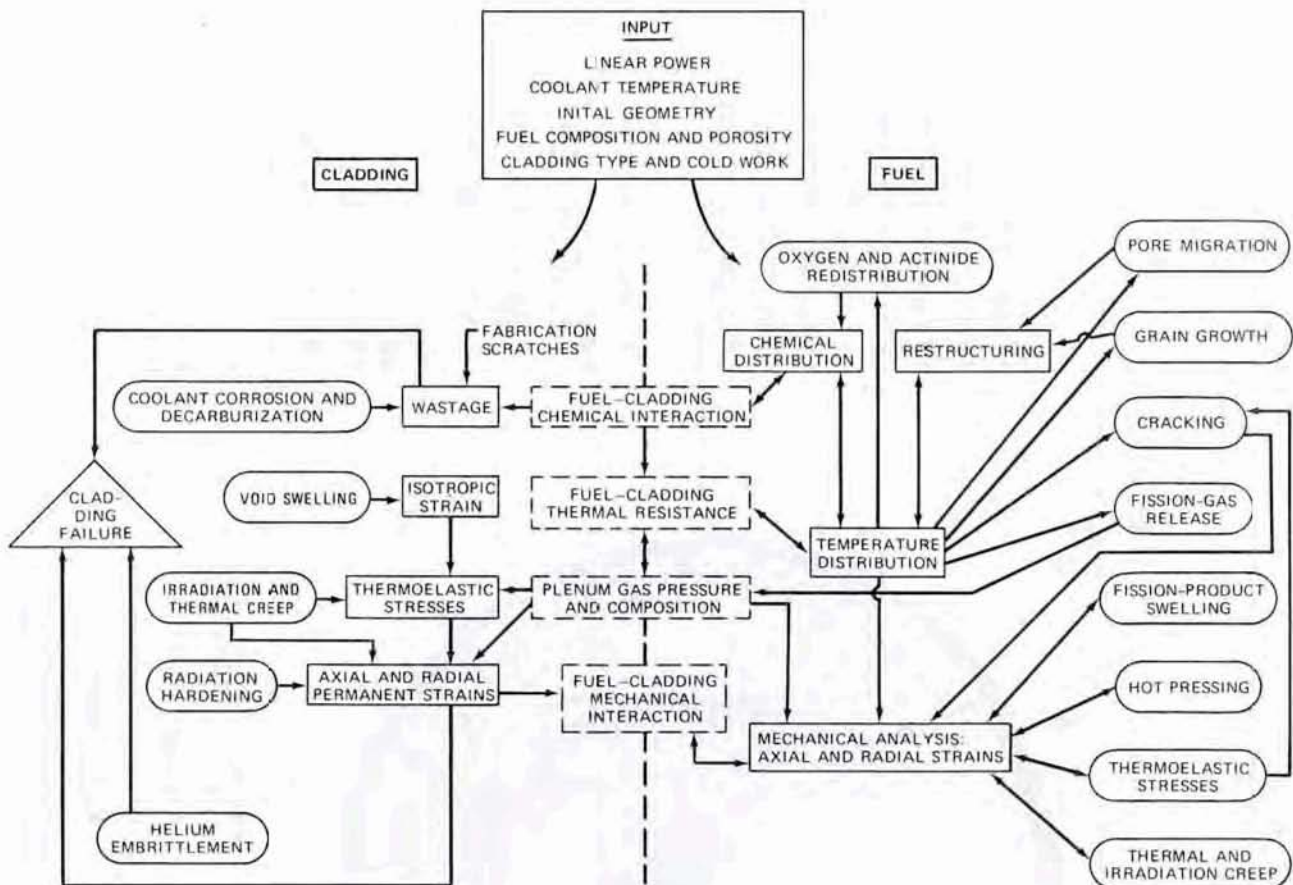
Fig. 21.1 Interrelation of mechanical, metallurgical, and chemical processes in fuel-element irradiation behavior.

radial nonuniformity introduced by actinide redistribution. Equations 10.47 and 10.48 are examples of the type of thermal-conductivity expressions used in thermal-analysis subroutines of fuel-modeling codes. The heat-source term in the conduction equation is given by Eq. 10.56. The temperature calculation also depends on the number and orientation of cracks in the fuel, on the size of the central void, and on the nature of the fuel—cladding gap. The temperature distribution depends sensitively on whether the gap is open or closed and whether it is filled with helium, fission gas, or liquid fission products.

21.1.2 Restructuring (Chap. 14)

The most important aspect of fuel restructuring in fast reactor fuel is the migration of the initial porosity of the fuel to the center by the process of vapor transport along the temperature gradient (Sec. 14.2). (Extensive fuel restructuring does not occur in light-water reactors, because the temperatures and temperature gradients are too small.) Equation 14.25 must be solved to describe the porosity redistribution phenomenon. The pore velocity is given by Eq. 14.11. The growth of equiaxed grains (Sec. 14.5) is important because grain size affects the creep strength of the fuel (Sec. 16.6). Other aspects of fuel restructuring are hot pressing (Sec. 16.11) which provides a means for

removing porosity in the equiaxed and unrestructured zones of the fuel, and fuel cracking. Figure 21.2 shows schematically the structural evolution of an oxide fuel during irradiation.
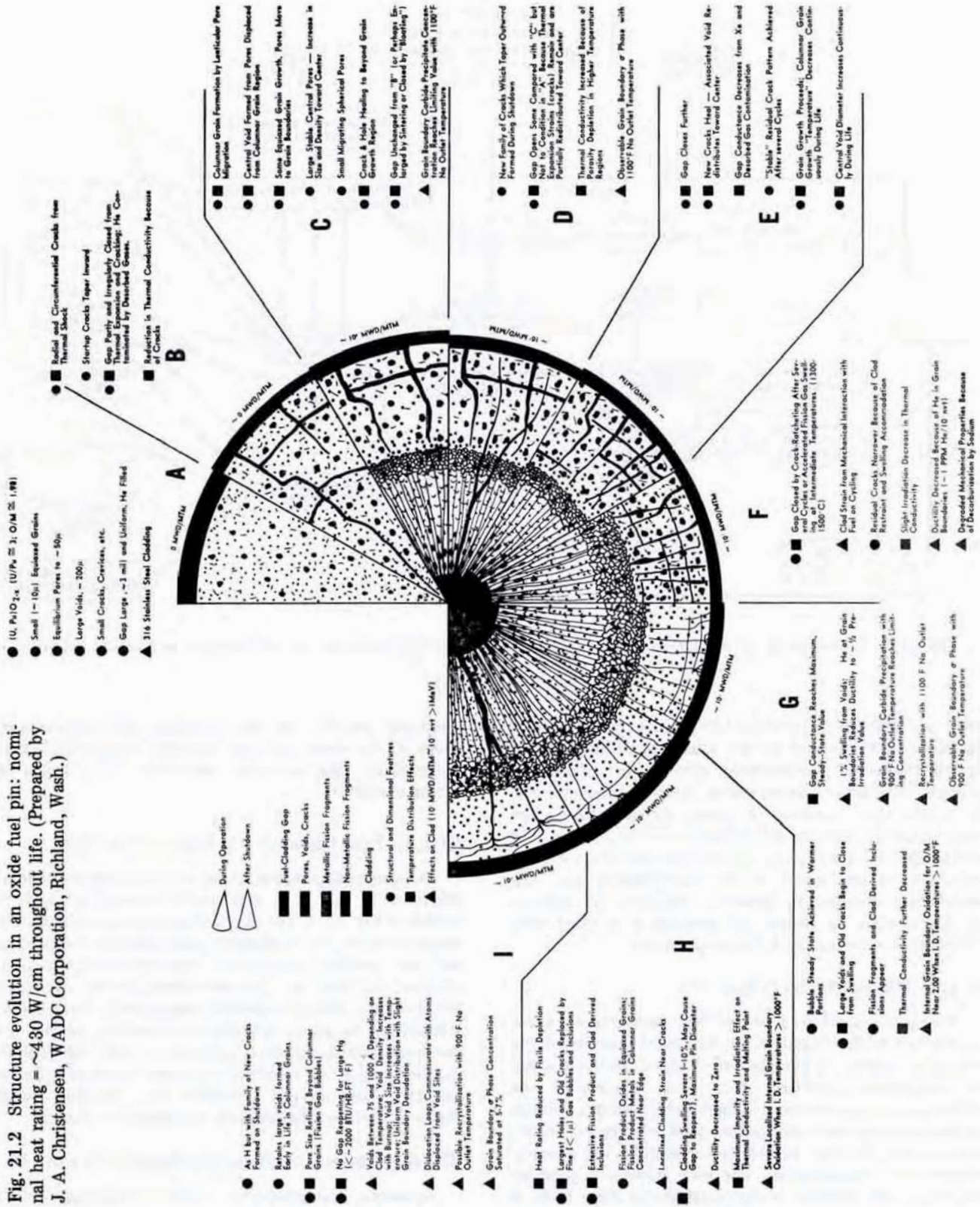
21.1.3 Fuel Chemistry (Chaps. 11 and 12)

Oxygen redistribution along the temperature gradient is described in Sec. 11.6, and actinide redistribution is described in Sec. 11.7. The chemical and physical states of the fission products, their migration under the thermal gradient, and the swelling caused by solid fission products are reviewed in Chap. 12. Chemical attack of the cladding by the fuel (Sec. 12.6) is especially important to fuel-modeling calculations because it contributes to cladding wastage (i.e., thinning) and to removal of oxygen from the fuel (by immobilization as cladding corrosion product). Burnup increases the oxygen available for cladding attack. Figure 21.3 shows the chemical evolution of a fuel pin.

21.1.4 Fission-Gas Behavior (Chaps. 13 and 15)

Accurate fuel modeling requires knowledge of the fraction of the stable fission gases which have been produced up to a particular time and which have been released to the plenum. The remaining fission gas is

Fig. 21.2 Structure evolution in an oxide fuel pin: nominal heat rating = ~430 W/cm throughout life. (Prepared by J. A. Christensen, WADC Corporation, Richland, Wash.)
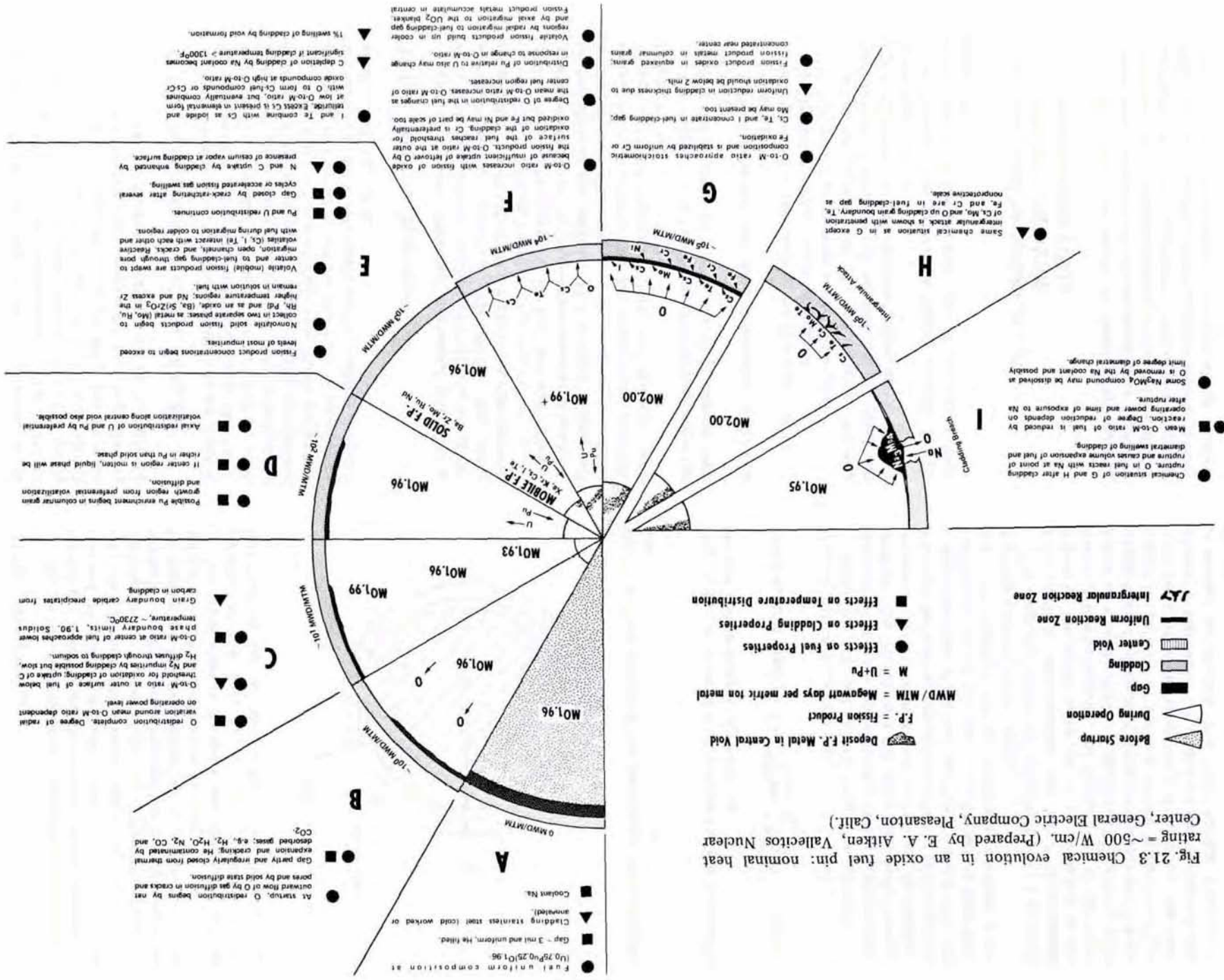
Fig. 21.3 Chemical evolution in an oxide fuel pin: nominal heat rating = ~500 W/cm. (Prepared by E. A. Aitken, Vallecitos Nuclear Center, General Electric Company, Pleasanton, Calif.)

Legend:

Before Startup
During Operation
Gap
Cladding
Center Void
Uniform Reaction Zone
Intergranular Reaction Zone

Deposit F.P. Metal in Central Void
F.P. = Fission Product
MWD/MTM = Megawatt days per metric ton metal
M = U+Pu

● Effects on Fuel Properties
▼ Effects on Cladding Properties
■ Effects on Temperature Distribution

Central regions:
MOBILE F.P. — Xe, Kr, Cs, I, Te
SOLID F.P. — Ba, Zr, Mo, Ru, Nd
U → Pu, Pu → U

MO1.93, MO1.96, MO1.99+, MO2.00, MO2.00, MO1.95, MO1.96, MO1.99

0 MWD/MTM, ~100 MWD/MTM, ~10³ MWD/MTM, ~10⁴ MWD/MTM, ~10⁵ MWD/MTM

Section A
● Fuel uniform composition at (U₀.₇₅Pu₀.₂₅)O₁.₉₆.
■ Gap ~3 mil and uniform, He filled.
▼ Cladding stainless steel (cold worked or annealed).
■ Coolant Na.

Section B
At startup, O redistribution begins by net outward flow of O by gas diffusion in cracks and pores and by solid state diffusion.
● ■ Gap partly and irregularly closed from thermal expansion and cracking; He contaminated by desorbed gases: e.g., H₂, H₂O, N₂, CO, and CO₂.

Section C
■ O redistribution complete. Degree of radial variation around mean O-to-M ratio dependent on operating power level.
▼ ■ O-to-M ratio at outer surface of fuel below threshold for oxidation of cladding; uptake of C and N₂ impurities by cladding possible but slow; H₂ diffuses through cladding to sodium.
▼ ● O-to-M ratio at center of fuel approaches lower phase boundary limits, 1.90, solidus temperature ~2730°C.
▼ Grain boundary carbide precipitates from carbon in cladding.

Section D
■ ● Possible Pu enrichment begins in columnar grain growth region from preferential volatilization and diffusion.
■ ● If center region is molten, liquid phase will be richer in Pu than solid phase.
■ ● Axial redistribution of U and Pu by preferential volatilization along central void also possible.

Section E
● Fission product concentrations begin to exceed levels of most impurities.
● Nonvolatile solid fission products begin to collect in two separate phases: as metal (Mo, Ru, Rh, Pd) and as an oxide, (Ba, Sr)ZrO₃ in the higher temperature regions; Nd and excess Zr remain in solution with fuel.
● Volatile (mobile) fission products are swept to center and to fuel-cladding gap through pores; migration, open channels, and cracks. Reactive volatiles (Cs, I, Te) interact with each other and with fuel during migration to colder regions.
■ ● Pu and U redistribution continues.
■ ● Gap closed by crack-ratcheting after several cycles or accelerated fission gas swelling.
▼ ● N and C uptake by cladding enhanced by presence of cesium vapor at cladding surface.

Section F
● O-to-M ratio increases with fission of oxide because of insufficient uptake of leftover O by the fission products. O-to-M ratio at the outer surface of the fuel reaches threshold for oxidation of the cladding; Cr is preferentially oxidized but Fe and Ni may be part of scale too.
● Degree of O redistribution in the fuel changes as the mean O-to-M ratio increases. O-to-M ratio of center fuel region increases.
● Distribution of Pu relative to U may also change in response to change in O-to-M ratio.
● Volatile fission products build up in cooler regions by radial migration to fuel-cladding gap and by axial migration to the UO₂ blanket. Fission product metals accumulate in central.
▼ 1% swelling of cladding under void formation.
▼ C depletion of cladding by Na coolant becomes significant if cladding temperature > 1300°F.
▼ ● C and Te combine with Cs as iodide and telluride. Excess Cs is present in elemental form at low O-to-M ratio, but eventually combines with O to form Cs-fuel compounds or Cs₂O oxide compounds at high O-to-M ratio.

Section G
● O-to-M ratio approaches stoichiometric composition and is stabilized by uniform Cr or Fe oxidation.
● Cs, Te, and I concentrate in fuel-cladding gap; Mo may be present too.
▼ Uniform reduction in cladding thickness due to oxidation should be below 2 mils.
● Fission product oxides in equiaxed grains; fission product metals in columnar grains concentrated near center.

Section H
● ▼ Same chemical situation as in G except intergranular attack is shown with penetration of Cs, Mo, and I-O up cladding grain boundary; Te, Fe, and Cr are in fuel-cladding gap as nonprotective scale.

Section I
Cladding Breach
● ■ Chemical situation of G and H after cladding rupture. O in fuel reacts with Na at point of rupture and causes volume expansion of fuel and diametral swelling of cladding.
● ■ Mean O-to-M ratio of fuel is reduced by reaction. Degree of reduction depends on operating power and time of exposure to Na after rupture.
● Some Na₃MoO₄ compound may be dissolved and probably removed by the Na coolant and possibly limit degree of diametral change.

contained in the fuel, and it may be desirable to be able to predict the size distribution of the fission-gas bubbles as a function of radial position in the fuel during irradiation. Although codes such as BUBL and GRASS (Sec. 13.12) were designed to do just this, they have not yet been incorporated into integral fuel-modeling codes, all of which use the crudest of gas-release and swelling models.

21.1.5 Cladding Behavior (Chaps. 18 to 20)

The most important effects of radiation on the cladding are void swelling (Chap. 19), irradiation creep (Sec. 19.7), and reduction in ductility (Chap18). Corrosion of the outer surface of the cladding and uniform decarburization by sodium in LMFBRs (Chap. 20) affect cladding strength and are included in the fuel-modeling codes. Radiation hardening (Secs. 18.4 to 18.8) can be important in determining the extent of plastic deformation of the cladding in regions of abnormally high stress.

21.1.6 Mechanical Properties

One of the most important mechanical properties of both fuel and cladding in the structural analysis is the thermal-expansion coefficient (Sec. 10.2). The creep properties of the fuel (thermal and irradiation) are reviewed in Chap. 16. Cladding thermal creep is governed by the same laws as thermal creep of the fuel, but with different numerical constants. The temperature variation of mechanical properties of the fuel (Secs. 16.2 and 16.3) is important because of the ~2000°C temperature change across the fuel radius during operation. As the temperature increases, Young's modulus approaches zero and Poisson's ratio approaches 1/2.

The output of a fuel-modeling calculation provides the detailed information as a function of irradiation time including:

1. The temperature and stress distribution in the fuel and cladding.

2. The extent of fuel cracking and fuel restructuring.

3. The fuel—cladding interfacial pressure.

4. The plenum gas pressure due to fission gases.

5. The net strain of the fuel and cladding, including the dilatational strain due to swelling and the radial and axial components of the permanent strains due to creep or plastic deformation.

6. The approach to fuel-pin failure, assessed, for instance, by the life-fraction rule (Sec. 18.11) or by a creep strain limit.

21.2 MECHANICAL MODELING OF FUEL-PIN BEHAVIOR (UNCRACKED FUEL)

In this section we review the stress—strain analysis, which, when combined with the materials input functions, determines the mechanical behavior of the fuel rod during irradiation. The fuel is assumed to remain free of cracks despite the fact that the thermal gradient induces stresses that exceed the fracture stress. The effect of fuel cracking on the analysis is considered in Sec. 21.3.

21.2.1 Gap Closure

One of the most important aspects of integral fuel-pin modeling is deciding whether or not the gap between the fuel and the cladding is closed or open. If the gap is open, only the plenum gas pressure loads the inside of the cladding and the outside of the fuel. If the gap is closed, the interaction force between the fuel and the cladding is due to contact of the two solids and is obtained only by mechanical analysis of the entire fuel pin.

The initial state of the pin is specified by the internal porosity of the fuel, P_0, and the thickness of the fuel—cladding gap in the as-fabricated element, t_{gap}°
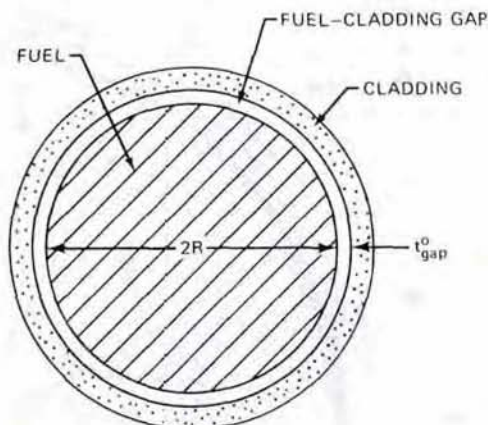
Fig. 21.4 Cross section of the fuel element before irradiation.

(Fig. 21.4). The smeared density of the fuel pin is related to the pore volume and the gap volume by

$$\text{Initial smeared density} = 1 - \frac{2\pi R t_{gap}^\circ + \pi R^2 P_0}{\pi (R + t_{gap}^\circ)^2} \qquad (21.1)$$

where R is the radius of the fuel.

When the fuel rod is first subject to neutrons and generates power, the temperature profile is approximately parabolic (Eq. 10.52), and the initial gap width changes because of thermal expansion of the fuel and the cladding. Although the thermal expansion coefficient of the cladding is larger than that of the fuel (see Figs. 10.8 and 10.9), the temperature rise of the fuel is considerably greater than that of the cladding. The net result is a reduction in the thickness of the gap upon startup.

The tangential strain of a cylindrical body is equal to the increase in radial position (i.e., radial displacement) divided by the initial radius (Eq. 21.5). According to the theory of thermoelasticity, the displacement of the outer surface of a solid cylinder is equal to $\alpha R \overline{T}$, where α is an average linear coefficient of thermal expansion and $\overline{T}$ is the average temperature of the solid, which is equal to $(T_0 + T_s)/2$ for a parabolic temperature distribution. The temperature change across the cladding is small compared with its average temperature. The initial hot-gap thickness is given by

$$\frac{t^{\circ}_{gap\,(hot)} - t^{\circ}_{gap\,(cold)}}{R} = \alpha_c T_c - \frac{1}{2}\alpha_f(T_0 + T_s) \quad (21.2)$$

where, for simplicity of notation, T_c, T_0, and T_s refer to the temperature rises of the cladding, fuel center line, and fuel surface, respectively, above the temperature at which the cold gap is measured ($\sim 25^{\circ}C$) and $R_{fuel} \cong R_{clad} = R$. Calculation of the initial hot-gapt thickness (or equivalently, of the fuel center line and surface temperatures) is a trial-and-error affair because of the dependence of the gap conductance on the gap thickness (see problem 10.2). When fuel cracking is included in the analysis, the hot-gap thickness is smaller than the value obtained from Eq. 21.2 (see Sec. 21.3). The initial cold-gap thickness is chosen so that the gap still exists on the initial rise to power. As fuel swelling due to fission products increases with irradiation time, the gap gradually closes and the fuel and cladding interact mechanically. Much later in the life of the fuel element, the gap may reopen because of cladding swelling (which does not vary linearly with fluence).

21.2.2 Mechanical Analysis

The fuel-element geometry used in fuel-modeling codes is shown in Fig. 21.5. The fuel and cladding are divided into a number of axial regions and radial intervals; each elementary volume considered in the analysis is shown as the ring on the right of Fig. 21.5. The original LIFE code[1,2] divided the fuel into three radial zones, corresponding to the columnar grain, equiaxed grain, and unstructured regions shown in Fig. 10.23, and put the entire cladding cross section into one radial zone. Recent work, however, has shown that the radial mesh must be much finer than three fuel zones and one cladding zone to properly account for the very steep radial temperature gradient in the fuel pin.

Other restrictions placed upon the analysis are:

1. The system is axisymmetric (i.e., there is no tangential variation of any variable).

2. Although both the fuel and the cladding may move axially (and not necessarily at the same rate), planes perpendicular to the z-direction in each material remain plane during deformation. This is the *plane strain* assumption. Friction is allowed between the fuel and cladding.

3. The time dependence inherent in the analysis (due to the swelling and creep phenomena) is handled by treating the system as a succession of equilibrium states.

4. The central void communicates with the plenum; so the inner radius of the fuel and the top of the uppermost axial zone are loaded by the plenum gas pressure.

5. The outer radius of the fuel and the inner radius of the cladding are loaded by the plenum pressure if the fuel—cladding gap is open and by the fuel—cladding interfacial pressure if the gap is closed.

6. The outer radius of the cladding is subject to the coolant pressure.

As a result of restrictions 1 and 2, only the normal stresses along the three principal directions in the cylindrical coordinate system are nonzero; these are denoted by σ_r, σ_θ, and σ_z and are positive if in tension. There are no shear stresses.

The governing relations for the mechanical analysis are similar to those presented for elastic deformations in the Appendix, except that the elastic strains given by Eq. A.21 must be supplemented by terms representing thermal expansion, swelling, and permanent deformations due to creep or plastic flow.

The equilibrium conditions given by Eqs. A.29 to A.31 are simplified by eliminating shear stresses and axial and tangential derivatives, which leads to the single relation

$$\frac{d\sigma_r}{dr} + \frac{\sigma_r - \sigma_\theta}{r} = 0 \quad (21.3)$$

Letting ϵ_r, ϵ_θ, and ϵ_z be the total strains in the three principal directions, the strain—displacement relations of Eq. A.32 become

$$\epsilon_r = \frac{du}{dr} \quad (21.4)$$

$$\epsilon_\theta = \frac{u}{r} \quad (21.5)$$

ϵ_z = constant with r except for discontinuity at
the fuel—cladding interface $\quad (21.6)$

where u is the radial displacement. Equations 21.4 and 21.5 satisfy the compatibility conditions (shown for Cartesian coordinates in Sec. A-3 of the Appendix) which precludes treating cracking of the fuel.

The total strain in each direction is divided into the categories shown in Table 21.1.

The elastic strains are given by Eqs. A.22 of the Appendix, with appropriate change in the coordinate system. The *constitutive relations* used in fuel-modeling analyses become

$$\epsilon_r = \frac{1}{E}[\sigma_r - \nu(\sigma_\theta + \sigma_z)] + \alpha T + \epsilon^s + \epsilon_r^c \quad (21.7)$$

$$\epsilon_\theta = \frac{1}{E}[\sigma_\theta - \nu(\sigma_r + \sigma_z)] + \alpha T + \epsilon^s + \epsilon_\theta^c \quad (21.8)$$

$$\epsilon_z = \frac{1}{E}[\sigma_z - \nu(\sigma_r + \sigma_\theta)] + \alpha T + \epsilon^s + \epsilon_z^c \quad (21.9)$$

Equations 21.7 to 21.9 apply to both the fuel and the cladding provided the linear thermal-expansion coefficient α, Young's modulus E, and Poisson's ratio ν are chosen accordingly and appropriate material functions are used for the swelling and creep/plastic strains in each part of the fuel element.

In the fuel, ϵ^s is given by

$$\epsilon_{fuel}^s = \frac{1}{3}\left[\left(\frac{\Delta V}{V}\right)_{solid\,fp} + \left(\frac{\Delta V}{V}\right)_{gaseous\,fp} - \left(\frac{\Delta V}{V}\right)_{hot\,pressing}\right] \quad (21.10)$$

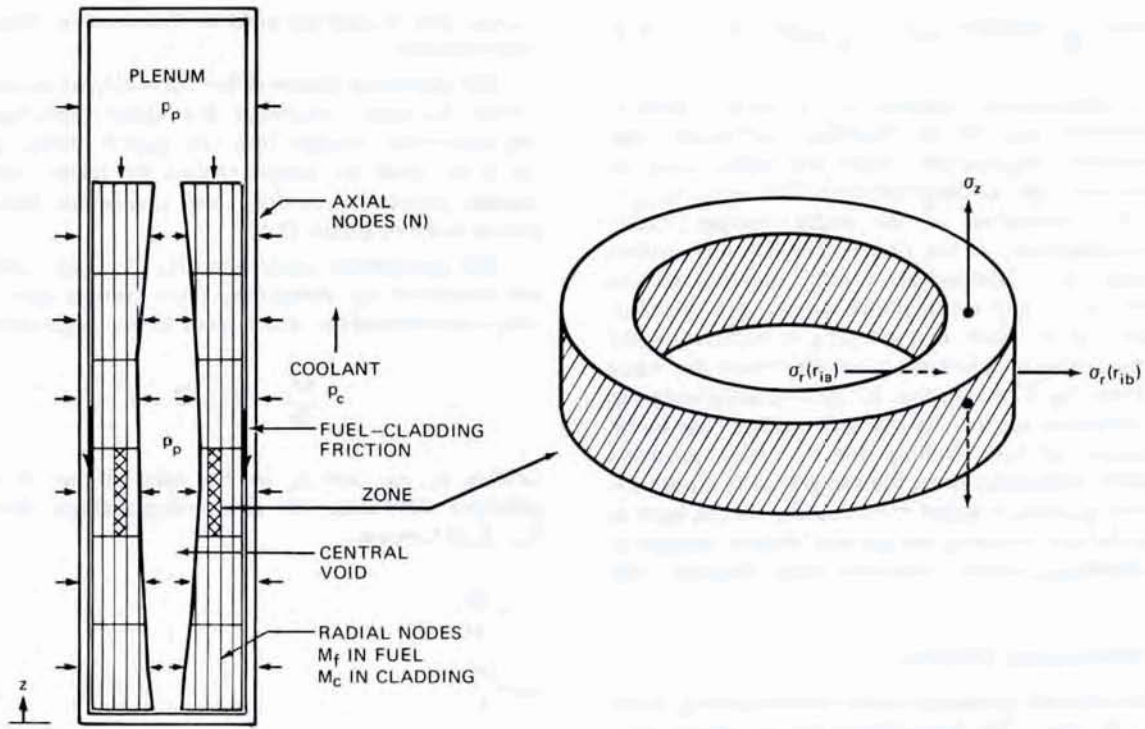Fig. 21.5 Subdivision of a fuel element into radial and axial zones for mechanical analysis.

Table 21.1 Components of the Total Strain

Component	Symbol	Isotropic?	Permanent?
Elastic	None	No	No
Thermal	αT	Yes	No
Swelling	ϵ^s	Yes	Yes
Creep/plastic	$\epsilon_r^c, \epsilon_\theta^c, \epsilon_z^c$	No	Yes

Equation 12.44 shows that the swelling due to solid fission products is proportional to burnup (or the rate of this swelling component is constant); the coefficient of proportionality depends only on fission-product yields and the partial volumes of the fission products.

The gaseous-fission-product swelling term is related to the size and concentration of fission-gas bubbles by Eq. 13.19. A model for $(\Delta V/V)_{\text{gaseous fp}}$ (either theoretical or empirical) must be supplied to the computation.

The hot-pressing contribution to fuel swelling is negative inasmuch as porosity is removed by this process. Typical hot-pressing kinetic formulas used in fuel-modeling analyses are given by Eqs. 16.177 and 16.190. The porosity P in these formulas must be interpreted as the cavity volume due to pores which do not contain fission gas rather than the total porosity.

In the cladding the swelling strain is due solely to void formation

$$\epsilon_{\text{clad}}^s = \frac{1}{3}\left(\frac{\Delta V}{V}\right)_{\text{void swelling}} \qquad (21.11)$$

where $(\Delta V/V)_{\text{void swelling}}$ can be determined from one of the theoretical models described in Sec. 19.6 or, more likely, by such empirical relations as Eq. 19.12.

The hydrostatic state of stress

$$\sigma_h = -\frac{1}{3}(\sigma_r + \sigma_\theta + \sigma_z) \qquad (21.12)$$

affects all the swelling terms in Eqs. 21.10 and 21.11 except that due to solid fission products (which is termed "inexorable"). Because the stresses in the fuel and cladding vary with time, swelling rate expressions $\dot{\epsilon}_{\text{fuel}}^s$ and $\dot{\epsilon}_{\text{clad}}^s$ are used instead of integrated swelling strains. The swelling rates are integrated along with the creep rates as the fuel-modeling code traces the evolution of the fuel pin during irradiation.

The permanent strains labeled ϵ_i^c ($i = r$, θ, or z) in Eqs. 21.7 to 21.9 are composed of creep and plastic deformations

$$\epsilon_i^c = \epsilon_i^{\text{creep}} + \epsilon_i^{\text{plastic}} \qquad (21.13)$$

Creep and plastic deformations occur at constant volume (unlike elastic deformation); so the components of ϵ^c are related by the incompressibility condition

$$\epsilon_r^c + \epsilon_\theta^c + \epsilon_z^c = 0 \qquad (21.14)$$

Formulation of the permanent strains based on the von Mises assumption that creep and plastic deformations occur only when the stress state deviates from pure hydrostatic

tension or compression (Sec. 18.3) leads to the stress—strain relations known as the Prandtl—Reuss flow laws or the Soderberg equations:

$$\epsilon_r^c = \left(\frac{\epsilon^*}{\sigma^*}\right)\left[\sigma_r - \frac{1}{2}(\sigma_\theta + \sigma_z)\right] \quad (21.15)$$

$$\epsilon_\theta^c = \left(\frac{\epsilon^*}{\sigma^*}\right)\left[\sigma_\theta - \frac{1}{2}(\sigma_r + \sigma_z)\right] \quad (21.16)$$

$$\epsilon_z^c = \left(\frac{\epsilon^*}{\sigma^*}\right)\left[\sigma_z - \frac{1}{2}(\sigma_r + \sigma_\theta)\right] \quad (21.17)$$

where σ^* and ϵ^* are the stress and strain deviators or the *equivalent stress* and *equivalent strain*, respectively, of the triaxial stress state

$$\sigma^* = \frac{1}{2^{1/2}}[(\sigma_r - \sigma_\theta)^2 + (\sigma_r - \sigma_z)^2 + (\sigma_\theta - \sigma_z)^2]^{1/2} \quad (21.18)$$

$$\epsilon^* = \frac{2^{1/2}}{3}[(\epsilon_r - \epsilon_\theta)^2 + (\epsilon_r - \epsilon_z)^2 + (\epsilon_\theta - \epsilon_z)^2]^{1/2} \quad (21.19)$$

Equations 21.15 to 21.17 and Eq. 21.19 can also be written in terms of the strain rates instead of the accumulated strains by placing dots over all the ϵ's. The creep/plastic stress—strain laws are of the same form as the elastic stress—strain relations (the first terms on the right-hand sides of Eqs. 21.7 to 21.9), but Young's modulus and Poisson's ratio in the stress—strain relations are replaced by σ^*/ϵ^* and $1/2$, respectively. The ratio σ^*/ϵ^* is called the creep or plasticity modulus of the material.

For deformation by creep, σ^*/ϵ^* can be obtained from the creep laws determined in uniaxial tests by replacing the uniaxial stress and strain by the equivalent stress and the equivalent strain. Thus the creep formula corresponding to the Nabarro—Herring model (Eq. 16.27) is

$$(\dot\epsilon^*)^{creep} = \frac{B\sigma^*}{d^2}\exp\left(-\frac{E_d}{kT}\right) \quad (21.20a)$$

where B is a constant, E_d is the activation energy for this form of creep, and d is the grain diameter. The parameters B and E_d are the same as those obtained in uniaxial creep tests.

For thermal creep controlled by dislocation climb, Eq. 16.87 is transformed to

$$(\dot\epsilon^*)^{creep} = B'(\sigma^*)^{4.5}\exp\left(-\frac{E_d'}{kT}\right) \quad (21.20b)$$

where B' and E_d' are constants determined by uniaxial creep tests.

Equations 21.20a and 21.20b refer to secondary or steady-state creep. Primary creep can be included in the analysis by a creep law that explicitly includes the time

$$(\dot\epsilon^*)^{creep} = K(\sigma^*)^n t^m \quad (21.21)$$

where K, n, and m are empirical constants.

Except for diffusional creep (Eq. 21.20), the creep moduli are functions of the state of stress (i.e., of σ^*).

Irradiation creep formulas (Eq. 16.132 for the fuel and Eqs. 19.176, 19.225, or 19.239 for the cladding) can be expressed in a similar fashion.

Plastic strain is expressed in analytical form suitable for programming by fitting the true stress—strain curves from tensile tests (e.g., the dashed curve in Fig. 18.11) by an equation of the form

$$(\epsilon^*)^{plastic} = a(\sigma^*)^b \quad (21.22)$$

where the constants a and b may be fixed by two points on the true stress—strain curve, e.g., the 0.2% offset yield point and the strain at the ultimate stress. For metals, the constants a and b depend on radiation hardening due to the fast-neutron flux. Plastic flow in the fuel is not currently considered in fuel modeling codes.

21.2.3 Solution for Radial Stresses and Displacements

The analysis up to this point is common to most fuel-modeling codes. If swelling and creep/plasticity were not considered, the problem would reduce to one of ordinary thermoelasticity for which analytical solutions are possible (see problems 21.1, 21.2, and 21.6 at the end of the chapter). However, the presence of time-dependent permanent strains and the sizeable variation of the mechanical properties of the fuel with position (mainly because of the radial temperature distribution) require numerical solution of the relevant equations. Moreover, the creep and swelling phenomena introduce time as a fundamental variable. The numerical solutions of the fuel-element structural behavior must not only deal with the spatial variation of the stresses and strains but with their time dependence as well. The various methods differ in the procedure for solving the set of equations, Eqs. 21.3 to 21.9. The technique described here is approximately that used in the LIFE code.[1]

The total strains ϵ_r and ϵ_θ are eliminated by combining Eqs. 21.7 to 21.9 with Eqs. 21.4 and 21.5, and the stresses are expressed in terms of the radial displacement

$$\sigma_r = \frac{E}{1+\nu}\left[\frac{du}{dr} + \frac{\nu}{1-2\nu}\left(\frac{du}{dr} + \frac{u}{r} + \epsilon_z - 3\alpha T - 3\epsilon^s\right)\right. \\ \left. - (\alpha T + \epsilon^s + \epsilon_r^c)\right] \quad (21.23)$$

$$\sigma_\theta = \frac{E}{1+\nu}\left[\frac{u}{r} + \frac{\nu}{1-2\nu}\left(\frac{du}{dr} + \frac{u}{r} + \epsilon_z - 3\alpha T - 3\epsilon^s\right)\right. \\ \left. - (\alpha T + \epsilon^s + \epsilon_\theta^s)\right] \quad (21.24)$$

$$\sigma_z = \frac{E}{1+\nu}\left[\epsilon_z + \frac{\nu}{1-2\nu}\left(\frac{du}{dr} + \frac{u}{r} + \epsilon_z - 3\alpha T - 3\epsilon^s\right)\right. \\ \left. - (\alpha T + \epsilon^s - \epsilon_r^c - \epsilon_\theta^c)\right] \quad (21.25)$$

Equations 21.23 and 21.24 are substituted into the equilibrium condition, Eq. 21.3, and the following differential equation for the radial displacement is obtained:

$$\frac{d}{dr}\left[\frac{1}{r}\frac{d(ru)}{dr}\right] = \left(\frac{1-2\nu}{1-\nu}\right)\left(\frac{d\epsilon_r^c}{dr} + \frac{\epsilon_r^c - \epsilon_\theta^c}{r}\right)$$

$$+ \left(\frac{1+\nu}{1-\nu}\right)\frac{d}{dr}(\alpha T + \epsilon^s) \quad (21.26)$$

The step leading to Eq. 21.26 requires that the elastic constants E and ν be assumed independent of r (and hence of temperature). This approximation is valid only when the radial interval over which the resulting equation applies is small. The elastic constants and all other temperature- and porosity-dependent quantities in the creep and swelling terms are evaluated at the average conditions in the radial zone over which Eq. 21.26 is integrated.

Equation 21.26 is applied to each ring in the fuel element (shown on the right-hand side of Fig. 21.5). Each ring is characterized by subscripts i and j, representing the radial and axial positions in the pin, respectively. In the fuel, the first radial zones (i = 1) form the boundary of the central void and the first axial zones (j = 1) are at the bottom of the fuel pin. In the cladding the first radial zone starts at the inner surface of the cladding. The number of axial zones (N) and radial zones (M_f in the fuel and M_c in the cladding) are chosen to balance speed of computing with accuracy. Equation 21.26 is integrated from the inner boundary of the *ith* radial zone (r_{ai}) to radial position r within the ring. If the mesh is sufficiently fine, Poisson's ratio may be assumed to be constant within the ring, and the radial displacement is

$$u(r) = \frac{C_{1i}}{r} + C_{2i}r + \left(\frac{1+\nu}{1-\nu}\right)\frac{1}{r}\int_{r_{ai}}^{r} r'(\alpha T + \epsilon^s)dr'$$

$$+ \frac{1}{2}\left(\frac{1-2\nu}{1-\nu}\right)\left[\frac{1}{r}\int_{r_{ai}}^{r}(\epsilon_r^c + \epsilon_\theta^c)\, r'dr'\right.$$

$$\left. + r\int_{r_{ai}}^{r}(\epsilon_r^c - \epsilon_\theta^c)\frac{dr'}{r'}\right] \quad (21.27)$$

where C_{1i} and C_{2i} are constants of integration for the *ith* zone which remain to be determined. At this point the LIFE code assumes that the thermal, swelling, and permanent strains are constant within each ring,* which reduces Eq. 21.27 to

$$u(r) = \frac{C_{1i}}{r} + C_{2i} + \left(\frac{1+\nu}{1-\nu}\right)[(\alpha T)_i + (\epsilon^s)_i]\frac{r^2 - r_{ai}^2}{2r}$$

_____

*The assumption of constant strain within each ring results in discontinuous changes in the strain from one ring to the next. This unrealistic result becomes less important as the number of radial rings into which the fuel element is divided becomes larger, but, in the original LIFE code, only four radial zones are used ($M_f = 3$, $M_c = 1$). In this case, the step changes in strain between rings produces incorrect final results in some cases. Rather than eliminate this discrepancy by increasing the number of radial zones, the strain components may be arbitrarily assigned the r-dependence $A + (B/r^2)$ within each ring, the constants A and B being determined by matching strains and strain gradients at ring boundaries.

$$+ \frac{1}{2}\left(\frac{1-2\nu}{1-\nu}\right)\left\{[(\epsilon_r^c)_i + (\epsilon_\theta^c)_i]\frac{r^2 - r_{ai}^2}{2r}\right.$$

$$\left. + [(\epsilon_r^c)_i - (\epsilon_\theta^c)_i]\, r\ln\frac{r}{r_{ai}}\right\} \quad (21.28)$$

where $(x)_i$ denotes the constant values of the strain components in ring i. The strains are also dependent on the axial position of the ring (denoted by j), but this description is omitted for clarity.

Since the radial boundary conditions needed to determine the integration constants apply to the radial stress component as well as to the displacement, Eq. 21.28 is substituted into Eq. 21.23, which leads to an equation for $\sigma_r(r)$ as a function of C_{1i}, C_{2i}, the strain components $(\alpha T)_i$, $(\epsilon^s)_i$, $(\epsilon_r^c)_i$, and $(\epsilon_\theta^c)_i$, the zone boundaries r_{ai}, and the axial strain ϵ_z.

The boundary condition at the inside of the central void at $r = r_0$ is

$$\sigma_r(r_0) = -p_p \quad (21.29)$$

where p_p is the plenum pressure. To ensure continuity of stress and displacement at the radial zone boundaries within the fuel, we have

$$\left.\begin{array}{l}\sigma_r(r_{i-1,b}) = \sigma_r(r_{ia}) \\[2mm] u(r_{i-1,b}) = u(r_{ia})\end{array}\right\} \quad (1 < i \le M_f) \quad (21.30)$$

The condition at the fuel–cladding interface depends on whether the gap is open or closed. For an open gap

$$\sigma_r(R) = -p_p \quad (21.31a)$$

For the outer fuel surface and the same condition for the inner surface at the cladding

$$\sigma_r(R) = -p_p \quad (21.31b)$$

If the gap is closed the conditions are

$$\sigma_r(R) = -p_{fc} \quad (21.32a)$$

in the fuel, and

$$\sigma_r(R) = -p_{fc} \quad (21.32b)$$

in the cladding. The fuel–cladding-interfacial pressure p_{fc} is yet to be determined.

The matching conditions within the cladding are expressed by

$$\left.\begin{array}{l}\sigma_r(r_{i-1,b}) = \sigma_r(r_{ia}) \\[2mm] u(r_{i-1,b}) = u(r_{ia})\end{array}\right\} \quad (1 < i \le M_c) \quad (21.33)$$

and at the outside of the cladding

$$\sigma_r(R + t_c) = -p_c \quad (21.34)$$

where p_c is the coolant pressure at the axial location where the radial integration is performed and t_c is the cladding thickness.

Since the boundary conditions were used to determine the integration constants C_{1i} and C_{2i} in each radial zone, the displacement distribution u(r) is now a function of:

1. The strain components $(\alpha T)_i$, $(\epsilon^s)_i$, $(\epsilon_r^c)_i$, and $(\epsilon_\theta^c)_i$ in each ring.

2. The axial strain ϵ_z, which may take on different values in the fuel and in the cladding.

3. The plenum pressure p_p and, if the fuel—cladding gap is closed, the interfacial pressure p_{fc}.

The dependence of u(r) on the axial strains of the fuel and cladding and on the interfacial pressure results from application of the boundary conditions. The radial displacements in the fuel and cladding may be written in the form

$$u_f\,[r, (\alpha T)_i, (\epsilon^s)_i, (\epsilon_r^c)_i, (\epsilon_\theta^c)_i, p_{fc}, \epsilon_{zf}] \quad (21.35a)$$

for $r_0 \leqslant r \leqslant R$ and $1 \leqslant i \leqslant M_f$, and

$$u_c\,[r, (\alpha T)_i, (\epsilon^s)_i, (\epsilon_r^c)_i, (\epsilon_\theta^c)_i, p_{fc}, \epsilon_{zc}] \quad (21.35b)$$

for $R \leqslant r \leqslant R + t_c$ and $1 \leqslant i \leqslant M_c$. At this juncture p_{fc} and the fuel and cladding axial strains ϵ_{zf} and ϵ_{zc} are unknown. Axial-force balances are needed for their computation.

21.2.4 Axial-Force Balances

Figure 21.6 shows that the axial forces acting on the stack of fuel between axial zone j and the upper surface of the fuel consist of the average axial stress, the plenum pressure, and the sum of the friction forces acting vertically on the outer surface of the fuel. These forces are positive if they restrict axial growth of the fuel and are zero if the fuel—cladding gap is open. The force balance on the hollow cylinder of fuel between the top of the stack and the dashed cross section in Fig. 21.6 is

$$-2\pi \int_{r_0}^{R} \sigma_z(r)\, r\, dr = \pi(R^2 - r_0^2)\, p_p$$

$$+ F + \sum_{k=j+1}^{N} F_k \quad (21.36)$$

The force balance on the cladding between the same axial location and the top of the fuel element is

$$-2\pi \int_{R}^{R+t_c} \sigma_z(r)\, r\, dr = \pi(R + t_c)^2\, p_{c(top)}$$

$$- \pi R^2\, p_p - F - \sum_{k=j+1}^{N} F_k \quad (21.37)$$

where $p_{c(top)}$ is the coolant pressure at the top of the fuel element.

The symbol F in the above equations is the axial friction force acting on the fuel—cladding interface at axial zone j. The subscript j has been omitted from the designation of the friction force, but the equations apply at each axial zone in the fuel element. The sums on the right-hand sides of Eqs. 21.36 and 21.37 are assumed to be
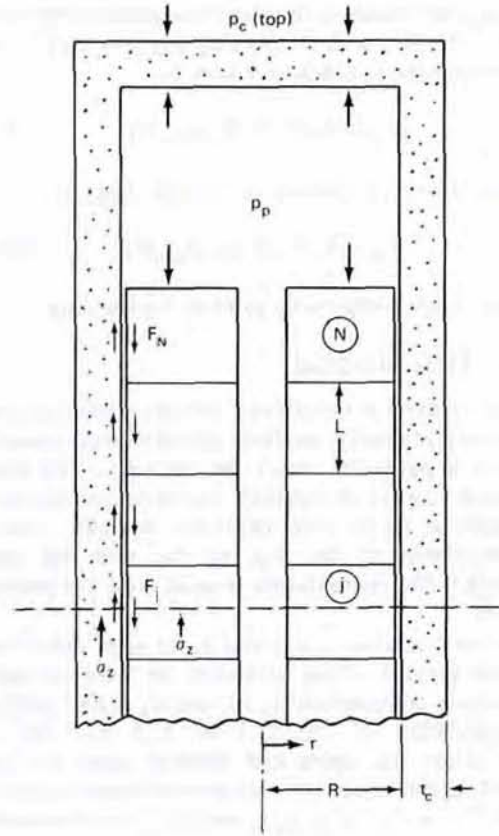
Fig. 21.6 Axial forces on the fuel and cladding.

known from previously completed computations on axial zones above zone j.

The axial stress distribution needed in the integrals in the force balances are given by inserting Eqs. 21.35 into Eq. 21.25. When the radial distribution of σ_z has been so used, Eqs. 21.36 and 21.37 can be solved for the axial strains in the fuel and cladding, ϵ_{zf} and ϵ_{zc}, in terms of

1. The radially averaged strain components $\overline{\alpha T}$, $\overline{\epsilon^s}$, $\overline{\epsilon_r^c}$, and $\overline{\epsilon_\theta^c}$ in the fuel and in the cladding.*
2. The fuel—cladding interfacial pressure p_{fc}.
3. The friction force F.

---

*Radial averages of the strain components, which are assumed to be constant in each ring, are defined for the fuel by

$$\bar{x} = \frac{1}{\pi(R^2 - r_0^2)} \sum_{i=1}^{M_f} (x)_i\, \pi(r_{ib}^2 - r_{ia}^2)$$

where r_{ia} and r_{ib} are the inner and outer radial boundaries of ring i and R and r_0 are the outer fuel and central void radii, respectively. In the cladding the radial average of a strain component is defined by

$$\bar{x} = \frac{1}{\pi[(R + t_c)^2 - R^2]} \sum_{i=1}^{M_c} (x)_i\, \pi(r_{ib}^2 - r_{ia}^2)$$

where t_c is the cladding thickness.

The axial force balances thus lead to equations for the axial strains in the fuel and in the cladding (see Ref. 1) which may be expressed in functional form by

$$\epsilon_{zf}[\overline{\alpha T}, \overline{\epsilon^s}, \overline{\epsilon_r^c}, \overline{\epsilon_\theta^c}, p_{fc}, F] \qquad (21.38a)$$

where the strain components refer to the fuel, and

$$\epsilon_{zc}[\overline{\alpha T}, \overline{\epsilon^s}, \overline{\epsilon_r^c}, \overline{\epsilon_\theta^c}, p_{fc}, F] \qquad (21.38b)$$

where the strain components refer to the cladding.

21.2.5 Time Stepping

Suppose the average stresses and the strain components due to creep/plasticity, swelling, and thermal expansion are known at a particular time t for the entire fuel element (i.e., for all rings at all heights). Calculation of the stresses and strains at $t + \delta t$ is accomplished one axial zone at a time, beginning at the top of the fuel and moving downward.* The computation at axial zone j is performed as follows.

The total strains ϵ_r, ϵ_θ, and ϵ_z in each radial ring at $t + \delta t$ are guessed. These estimates are used to generate average stress components $\overline{\sigma}_r$, $\overline{\sigma}_\theta$, and $\overline{\sigma}_z$ in each radial ring by manipulation of Eqs. 21.7 to 21.9 (see Ref. 1 for details). Since the creep and swelling rates are known functions of the stress, the component strains in each ring at $t + \delta t$ [i.e., $(\alpha T)_i$, $(\epsilon^s)_i$, $(\epsilon_r^c)_i$, and $(\epsilon_\theta^c)_i$] can be calculated from the average stress components just determined. These strain components are then used in the radial displacement equation (Eqs. 21.35). Similarly, the same strain components are radially averaged and used in Eqs. 21.38 to obtain first estimates of the axial strains at $t + \delta t$.

The quantities of interest are the changes in ϵ_{zf} and ϵ_{zc} during the interval between t and $t + \delta t$. These differences are obtained by subtracting the known axial strains at time t from those calculated by the method described in the preceding paragraph:

$$\delta\epsilon_{zf}(p_{fc}, F) = \text{change in axial strain of fuel}$$
$$\text{in time } \delta t \qquad (21.39)$$

$$\delta\epsilon_{zc}(p_{fc}, F) = \text{change in axial strain of cladding}$$
$$\text{in time } \delta t \qquad (21.40)$$

Similarly the changes in the radial displacements of the fuel outer surface and the cladding inner surface during δt can be expressed in the following functional form:

$$\delta u_{Rf}(p_{fc}, \epsilon_{zf}) = \text{change in radial displacement of}$$
$$\text{fuel outer surface in time } \delta t \qquad (21.41)$$

$$\delta u_{Rc}(p_{fc}, \epsilon_{zc}) = \text{change in radial displacement of}$$
$$\text{cladding inner surface in time } \delta t \qquad (21.42)$$

Equations 21.39 to 21.42 are used to determine p_{fc} and F at $t + \delta t$. First, however, it must be ascertained whether the

---

*In the LIFE code the calculation begins at the bottom of the fuel column.

gap opens up or remains closed in δt. It is assumed that the gap is closed at time t.

1. Assume the gap opens up in time δt: Set $F = 0$, replace p_{fc} by p_p, and determine the axial strain changes of the fuel and the cladding from Eqs. 21.39 and 21.40 wherein the two arguments are both zero. Substitution of the axial strains at $t + \delta t$ into Eqs. 21.41 and 21.42 determines the radial displacements of the fuel outer surface and of the cladding inner surface. If $\delta u_{Rc} > \delta u_{Rf}$, the original assumption is correct, and the gap has in fact opened in the time interval δt. If the calculated fuel displacement is greater than the calculated cladding displacement, the gap remains closed and procedure 2 is used.

2. The gap remains closed in time δt: If fuel—cladding contact is maintained, the radial displacement of the fuel outer surface must equal that of the cladding inner surface, or

$$\delta u_{Rf} = \delta u_{Rc} \qquad (21.43)$$

To complete the problem, we must determine whether the fuel and the cladding are so tightly wedged together that they move in unison (axially) during the interval δt (the stick condition) or whether the frictional force is large enough to permit relative axial displacement (the slip condition).

(a) The stick condition: If the fuel and the cladding stick, then the change in fuel axial strain during δt is equal to the change in the cladding axial strain, or

$$\delta\epsilon_{zf} = \delta\epsilon_{zc} \qquad (21.44)$$

Since the changes in strain in the fuel and cladding are functions of p_{fc} and F according to Eqs. 21.39 and 21.40, Eq. 21.44 is equivalent to a relation between p_{fc} and F. If a value of p_{fc} is selected, F is computed by the relation between these two variables implicit in Eq. 21.44, and then $\delta\epsilon_{zf}$ and $\delta\epsilon_{fc}$ are individually computed from Eqs. 21.39 and 21.40. Since the values of the fuel and cladding axial strains at the beginning of the interval are known, the axial strains at $t + \delta t$ can be computed from the values of the $\delta\epsilon_{zf}$ and $\delta\epsilon_{zc}$ just determined. With ϵ_{zf} and ϵ_{zc} at $t + \delta t$ known for the selected p_{fc}, the displacement changes δu_{Rf} and δu_{Rc} can be determined from Eqs. 21.41 and 21.42. The value of p_{fc} which causes Eq. 21.43 to be satisfied is the correct one. By this method, p_{fc} and F can both be determined if the fuel and cladding stick during the time interval δt.

To determine whether the p_{fc} and F values so calculated are compatible, we can also compute F from the definition of the coefficient of static friction, μ_{sf}. Sticking occurs if

$$F < \mu_{sf}(2\pi RL) p_{fc} \qquad (21.45)$$

where L is the height of an axial zone. The coefficient of static friction of UO_2 and stainless steel is taken as ~0.8. If the value of F does not satisfy Eq. 21.45, the frictional force is so large that the fuel and cladding cannot stick together; instead, they slip.

(b) The slip condition: If the fuel and the cladding slip relative to each other in the time interval δt, F and p_{fc} are taken to be related by the coefficient of sliding friction, μ_{sl}

$$F = \mu_{sl}(2\pi RL)\, p_{fc} \qquad (21.46)$$

Using Eq. 21.46 in Eqs. 21.39 and 21.40, we can compute values of $\delta\epsilon_{zf}$ and $\delta\epsilon_{zc}$ (they are no longer equal) for each interfacial pressure selected. The value of p_{fc} and the associated values of ϵ_{zf} and ϵ_{zc} at $t + \delta t$ are used in Eqs. 21.41 and 21.42 to give δu_{Rf} and δu_{Rc}. The p_{fc} value that satisfies Eq. 21.43 is the solution.

Whichever condition (open, stick, or slip) applies over the interval δt, the quantities p_{fc}, F, ϵ_{zf}, and ϵ_{zc} are determined at time $t + \delta t$ for the particular axial zone under consideration by method 1, 2a, or 2b. Thus the radial displacement distributions given by Eqs. 21.35 are determined at $t + \delta t$ because the strain components contained therein have been supplied by the initial guesses and p_{fc}, ϵ_{zf}, and ϵ_{zc} have been determined in terms of these same guesses by the technique just outlined. To assess the accuracy of the guesses of the total strains which began the iteration, we compute the following radially averaged total-strain components:

$$\bar{\epsilon}_r = \frac{1}{\pi(R^2 - r_0^2)} \int_{r_0}^{R} \left(\frac{du}{dr}\right) 2\pi r\, dr \qquad (21.47a)$$

and

$$\bar{\epsilon}_\theta = \frac{1}{\pi(R^2 - r_0^2)} \int_{r_0}^{R} \left(\frac{u}{r}\right) 2\pi r\, dr \qquad (21.47b)$$

for the fuel and analogous integrals for the cladding.

The average total-strain components in the fuel and the cladding at the end of the time step given by Eqs. 21.47 are compared with the initial guesses. The computation is repeated using better initial guesses of the total strains until a consistent set of stresses and strains at $t + \delta t$ are obtained.

After convergence at axial zone j, the code moves to the next axial region, and the entire radial iteration procedure is begun again. When the bottom of the fuel pin is reached, the time step is advanced, and the cycle is repeated.

The computation ceases when the desired irradiation history is completed or when the cumulative damage index of the cladding equals unity. A flow chart of the LIFE fuel-modeling code (which also includes cracking) is shown in Fig. 21.7.

21.3 FUEL CRACKING

Immediately upon startup and before swelling or creep has occurred to any appreciable extent, the fuel develops a network of cracks oriented either along radial planes passing through the fuel-pin axis (sometimes called θ cracks because they are perpendicular to the θ direction) or along horizontal planes perpendicular to the z-axis (z cracks). These cracks appear because the thermoelastic stress components exceed the fracture strength of the fuel in tension (Fig. 16.7). The parabolic temperature gradient in the fuel
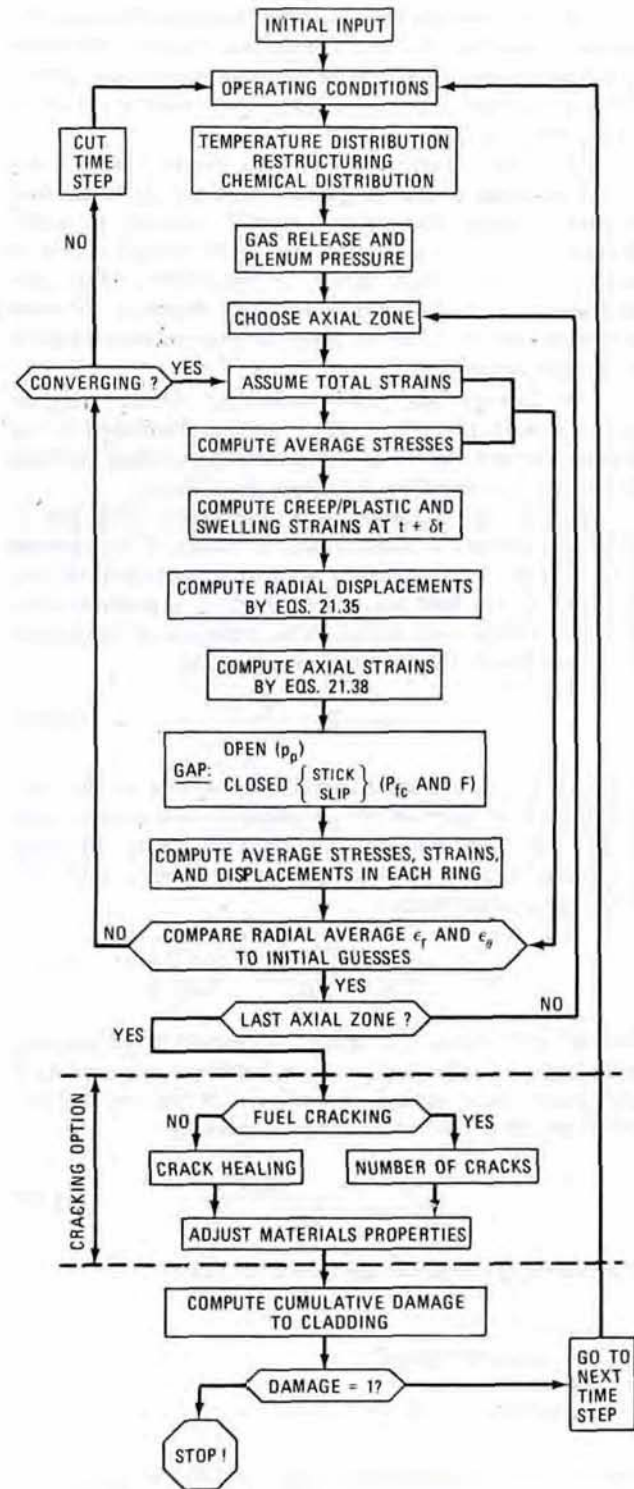
Fig. 21.7 Flow chart of the LIFE fuel-modeling code. (After Ref. 2.)

induces tensile stresses in the θ- and z-directions in the outer region of the fuel where the fuel is brittle (because $T < \sim1400°C$). In the inner core of the fuel, the thermal stresses are compressive, and, because the strength in compression is an order of magnitude greater than the tensile

strength, no cracking occurs in the interior. Moreover, the inside of the fuel is above the ductile-to-brittle transition temperature and therefore can sustain appreciable plastic deformation before fracture. Additional cracking occurs on each power change.

The thermal stress in the cladding due to the temperature drop through this component does not cause cladding cracking because the metal is ductile (initially at least). However, the thermal stresses can result in plastic flow at startup if the linear power is sufficiently large (see problem 21.2 at end of chapter) and continue to cause permanent deformation by creep through power operation of the fuel element.

The fuel-cracking phenomenon at startup may be analyzed with the aid of the equations developed in the previous section, which in the absence of swelling or creep strains can be treated by thermoelasticity theory.

Consider an infinitely long cylindrical fuel pin of radius R operated at linear power $\mathscr{P}$ W/cm. If the thermal conductivity of the matrix is assumed independent of temperature, fission heat generation results in a parabolic temperature profile (Eq. 10.52). The temperature drop from the center line to the fuel surface is given by

$$T_0 - T_s = \frac{\mathscr{P}}{4\pi\bar{k}} \tag{21.48}$$

where $\bar{k}$ is the average thermal conductivity of the fuel. Application of thermoelasticity theory to this situation (see problem 21.1 at end of the chapter) shows that the tangential or hoop stress in the fuel, σ_θ, varies with fractional radius according to

$$\sigma_\theta = -\frac{\alpha E \mathscr{P}}{16\pi(1-\nu)\bar{k}}\left[1 - 3\left(\frac{r}{R}\right)^2\right] \tag{21.49}$$

Stresses are positive if in tension. Equation 21.49 indicates compression of the fuel out to a fractional radius of $1/3^{\frac{1}{2}}$ and tensile hoop stresses thereafter. The maximum stress, which occurs at the outer surface, is given by

$$(\sigma_\theta)_{max} = \frac{\alpha E \mathscr{P}}{8\pi(1-\nu)\bar{k}} \tag{21.50}$$

The following properties are typical of UO_2:

$\alpha = 10^{-5}$ °C^{-1}
$E = 1.4 \times 10^8$ kN/m^2
$\nu = 0.3$
$\bar{k} = 0.028$ W cm^{-1} °C^{-1}

From Fig. 16.7 the fracture stress of UO_2 is ~1.5 × 10^5 kN/m^2. Application of Eq. 21.50 shows that the fracture stress is attained at the outer surface of the fuel pin when the linear power is ~50 W/cm. Since this value is an order of magnitude lower than the normal linear power of an operating fuel pin (Table 10.2), it is evident that extensive cracking of the brittle outer portion of the fuel is unavoidable. The cracks due to the tangential stress occur on planes emanating in radial directions from the center and containing the fuel-pin axis. The cracks shown in Fig. 16.8 are of this variety. The radial cracks extend into the fuel to a distance at which the tangential stress given by Eq. 21.49 becomes equal to the fracture stress, provided the temperature at this point is below the brittle-to-ductile transition. Because the maximum axial tensile stress is also given by Eq. 21.50, cracks on fuel cross sections perpendicular to the pin axis can also occur.

One of the most important functions of fuel cracking is to move void volume from the fuel—cladding gap to the interior of the fuel in the form of spaces between the cracked surfaces. Consider fissures along radial planes in the fuel (i.e., θ cracks). When the fuel cracks, the tangential stress at the crack location vanishes, and the two surfaces of the crack separate slightly because of the tensile hoop stresses in the interior of the wedges of solid which are separated by cracks. Since the solid is nearly incompressible, crack opening is accompanied by radially outward movement of the solid in the wedges. The temperature distribution remains parabolic throughout the fuel after cracking has occurred because heat does not flow in the θ direction when the cylinder is intact, and radial gaps, to first approximation, do not perturb the heat flow lines. The thermoelastic stresses in the cracked fuel, however, are no longer axially symmetric; σ_θ is zero at the crack surface but not in the interior of the cracked pieces. Consequently the formulas used in the preceding section are no longer applicable because they neglected tangential derivatives of the stresses and strains and did not consider shear stresses. Nevertheless, an approximate calculation of the tangential strain, $\Delta R/R$, which results from cracking in a parabolic temperature distribution is given below.

Suppose the radial cracks extend from the periphery of the fuel to radial position R_c. Since the tangential strain of the outer surface of a solid cylinder is $\alpha\bar{T}$, where $\bar{T}$ is the average temperature, the tangential strain of the solid portion of the fuel pin between the center and R_c is

$$\frac{\Delta R_c}{R_c} = \frac{1}{2}\alpha(T_0 + T_c)$$

where T_0 and T_c are the central temperature and the temperature at the root of the crack, respectively (both are measured above ambient temperature). The thickness in the radial direction of the wedges that result from cracking of the outside of the cylinder is $L_c = R - R_c$, where R is the radius of the fuel. We approximate the strain of these blocks of solid in the direction of the temperature gradient as the product of the linear coefficient of expansion and the average temperature of the wedges, or

$$\frac{\Delta L_c}{L_c} = \frac{1}{2}\alpha(T_c + T_s)$$

where T_s is the difference between the surface temperature of the fuel and ambient temperature. The total radial displacement, $\Delta R = \Delta R_c + \Delta L_c$, is given by the preceding two equations:

$$\Delta R = \frac{1}{2}\alpha\left[R_c(T_0 + T_c) + L_c(T_c + T_s)\right]$$

$$= \frac{1}{2}\alpha R\left[\left(\frac{R_c}{R}\right)T_0 + T_c + \left(\frac{R - R_c}{R}\right)T_s\right]$$

For a parabolic temperature distribution, $T_c = T_0 - (T_0 - T_s)(R_c/R)^2$, or the above formula can be written as

$$\frac{\Delta R}{R} = \frac{1}{2}\alpha[(1 + \eta_c - \eta_c^2)T_0 + (1 - \eta_c + \eta_c^2)T_s] \quad (21.51)$$

where $\eta_c = R_c/R$ is the fractional radius at which the cracks begin. When no cracking occurs ($\eta_c = 1$), Eq. 21.51 reduces to the strain formula used in determining the hot-gap thickness (Eq. 21.2). If the fuel fracture strength is zero, Eq. 21.49 shows that the crack roots start at $\eta_c = 1/3^{\frac{1}{2}}$. For $T_0 = 2500 - 300 = 2200°K$, $T_s = 1000 - 300 = 700°K$, and $\alpha = 1 \times 10^{-5}\ °K^{-1}$, the fractional increases of the fuel radius due to thermal stresses in the cracked and uncracked portions of the fuel are

$$\left(\frac{\Delta R}{R}\right)_{cracked} = 5 \times 10^{-6}[(1.24)(2200)$$
$$+ (0.76)(700)] = 0.0163$$

and

$$\left(\frac{\Delta R}{R}\right)_{uncracked} = 5 \times 10^{-6}(2200 + 700) = 0.0145$$

This difference in tangential strain arises from the inability of the cracked outer annulus to contain the expansion of the hot fuel in the interior of the pellet. The larger expansion of cracked fuel compared to uncracked solid reduces the fuel—cladding gap at startup below the value computed from Eq. 21.2 (by about 10%).

The effect of cracking on the mechanical performance of the fuel cannot be exactly taken into account in the fuel-modeling codes described in the previous section. To do so would require (1) knowledge of the precise location and size of every crack in the fuel and (2) solution of the complete three-dimensional stress—strain problem in each of the blocks of intact solid without the aid of the major simplification afforded by the assumption of symmetry around the central axis which is used in the derivation of Sec. 21.2. Consequently the phenomenon is modeled by assuming that cracking occurs only on the principal planes (specifically only θ and z cracks are considered). The effect of multiple cracking is treated in a manner that retains the cylindrical symmetry of the system in a macroscopic sense. Rather than treat a solid containing a population of discrete fissures, an equivalent continuous solid body with directionally dependent elastic constants is used in the stress analysis.[2,10] The properties of this nonisotropic but homogeneous medium are governed by the type and number of cracks in the real solid.

Suppose cracking occurs along radial planes (θ cracks). It is intuitively expected that the fuel would be weakened in the θ-direction but would retain essentially the solid-body strength in the other two principal directions. To reproduce this effect in the homogenized model of the cracked solid, we reduce Young's modulus in Eq. 21.8 from E to a lower value denoted by E'. At the same time, we decrease Poisson's ratio for all $r\theta$ and $z\theta$ contractions from ν to ν'. The constitutive equations in the cracked regions of the fuel assume the form

$$\sigma_r = \frac{1}{E}(\sigma_r - \nu'\sigma_\theta - \nu\sigma_z) + \alpha T + \epsilon^s + \epsilon_r^c \quad (21.52)$$

$$\sigma_\theta = \frac{1}{E'}(\sigma_\theta - \nu'\sigma_r - \nu'\sigma_z) + \alpha T + \epsilon^s + \epsilon_\theta^c \quad (21.53)$$

$$\sigma_z = \frac{1}{E}(\sigma_z - \nu\sigma_r - \nu'\sigma_\theta) + \alpha T + \epsilon^s + \epsilon_z^c \quad (21.54)$$

Using these constitutive relations in cracked portions of the fuel represents an attempt to compensate for the fact that the compatibility conditions (Eqs. 21.4 and 21.5) are not applicable in the real solid. However, analysis of the cracked fuel starting from Eqs. 21.52 to 21.54 retains the axial symmetry and freedom from shear stresses characteristic of the treatment of the intact solid. The result of using the modified constitutive relations along with the equilibrium and strain—displacement equations is a differential equation for the radial displacement similar to Eq. 21.26 but containing additional terms reflecting the difference in the primed and unprimed elastic constants in Eqs. 21.52 to 21.54.

A set of constitutive relations similar to Eqs. 21.52 to 21.54 for fuel with θ cracks can be developed for horizontally cracked fuel or for simultaneous cracking perpendicular to both the θ- and z-directions.

The new set of constitutive relations and the resulting displacement equation is applied to the cylindrical rings into which the fuel has been divided (Fig. 21.5) whenever the stresses σ_θ or σ_z exceed the fracture stress in tension (Fig. 16.7). The LIFE code (Fig. 21.7) checks for cracking after each time step. Multiple cracking in a ring can occur if the linear power changes or simply from the constant power evolution of the stress distributions in the fuel. One crack is added to the ring each time the fracture stress is exceeded at a particular location. On the other hand, cracks may be removed by healing if the stress in the ring remains compressive for a sufficient duration of time. The fundamental study of crack healing is in its infancy; quantitatively expressible mechanisms of this process are not yet available, although some experiments designed to elucidate crack healing have been performed.[11,12] In the LIFE code[2] cracks are considered to have healed whenever the appropriate stress component in a ring with $T > 1400°C$ is compressive and is applied continuously for at least 1 hr.

Application of the nonisotropic but homogeneous model of a cracked region of the fuel requires input of the modified elastic constants E' and ν'. In the LIFE calculation the reduction in elastic constants in the directions weakened by cracking is taken as

$$E' = \left(\frac{2}{3}\right)^N E \quad (21.55)$$

$$\nu' = \left(\frac{1}{2}\right)^N \nu \quad (21.56)$$

where N is the number of cracks in the particular direction. Although an attempt is made in Ref. 2 to justify these

formulas on theoretical grounds, the analysis, and in fact the entire treatment of cracking in fuel-modeling codes, is on a rather tenuous basis; the use of Eqs. 21.52 to 21.54 in conjunction with Eqs. 21.55 and 21.56 can only be justified by the success of the fuel-modeling code in reproducing computationally the observed structural changes in irradiated fuel.

21.4 FUEL-ELEMENT DEFORMATIONS DURING IRRADIATION

21.4.1 Cladding Strains

Although the fuel-modeling codes described in the preceding three sections of this chapter calculate the stress and strain patterns in both the fuel and the cladding in great detail, very few of these predictions are amenable to comparison with experimental measurements. Assessment of code accuracy and code calibration usually relies on comparison of the performance predictions with the following characteristics of a fuel element as determined by postirradiation examination of fuel rods in a hot cell:

1. Permanent diametral, or tangential, strain of the cladding as a function of axial position along the fuel rod. This measurement corresponds to the code prediction of $\epsilon^s + \epsilon_\theta^c$ (the inelastic or irreversible strains) of the last radial ring in the cladding at the end of irradiation.

2. Cladding swelling due to void formation, which corresponds to $3\epsilon^s$ in the code. Void swelling may be measured by the immersion method or by transmission electron microscopy (see Sec. 19.2), although the latter technique is too time-consuming for investigation of a large number of samples of irradiated cladding.

3. Postirradiation microscopic examination of cross sections of the irradiated fuel pin provides qualitative information on the extent of restructuring of the fuel and can indicate whether or not the fuel—cladding gap was open at the time of shutdown. The cracks observed in such examinations (e.g., Fig. 10.23), however, are cooling cracks and do not represent the cracks present in the fuel during irradiation.

Specially instrumented fuel elements can supply information on diametral strains as well as axial elongation of both the fuel and the cladding during operation. The diametral strains measured in-pile include elastic deformation and thermal expansion, both of which disappear when the power is turned off. In-pile structural measurements have been performed primarily in thermal facilities using light-water reactor fuel rods.[13]

The inelastic component ϵ_θ^c of the strain at the time of shutdown is determined by subtracting the measured swelling strain from the total strain. This inelastic-strain component is one of the indicators of cladding damage and approach to failure. Indeed, operating limits on LMFBR fuel pins may be given as a maximum allowable permanent diametral strain not including void swelling. The latter is not believed to affect the rupture lifetime of the cladding.

During normal operation the primary contribution to the inelastic strain ϵ_θ^c is due to creep and very little is due to plastic deformation. However, $(\epsilon_\theta^c)^{creep}$ itself consists of

two components, thermal creep and irradiation creep. The irradiation creep may or may not be damaging to the cladding. Even though thermal-creep strain is probably the principal source of cladding damage and ultimately leads to failure, there is no way of dividing the measured cladding creep strain into thermal- and irradiation-induced components. This distinction, however, is easily made in the fuel-modeling code, although the accuracy of the prediction is difficult to gauge.

Figure 21.8 shows the LIFE code predictions of swelling and inelastic strain of a stainless-steel-clad mixed-oxide fuel rod that had been irradiated in a fast reactor.[14] The circle on the graph represents the measured diametral strain in the cladding at the axial location of peak linear power. The seemingly excellent agreement between the code prediction of ϵ_θ^c and the single datum is not to be construed as a measure of the reliability of the theoretical models embodied in LIFE. The code had previously been fine tuned on the basis of other cladding strain data because, when first applied to the fuel element represented by Fig. 21.8, the calculated cladding inelastic strain was a factor of 2 larger than the measurement. Therefore the code was recalibrated by adjusting the input materials constants (in this case, the fission-gas swelling rate, which was decreased by a factor of 4) to force agreement of the computation
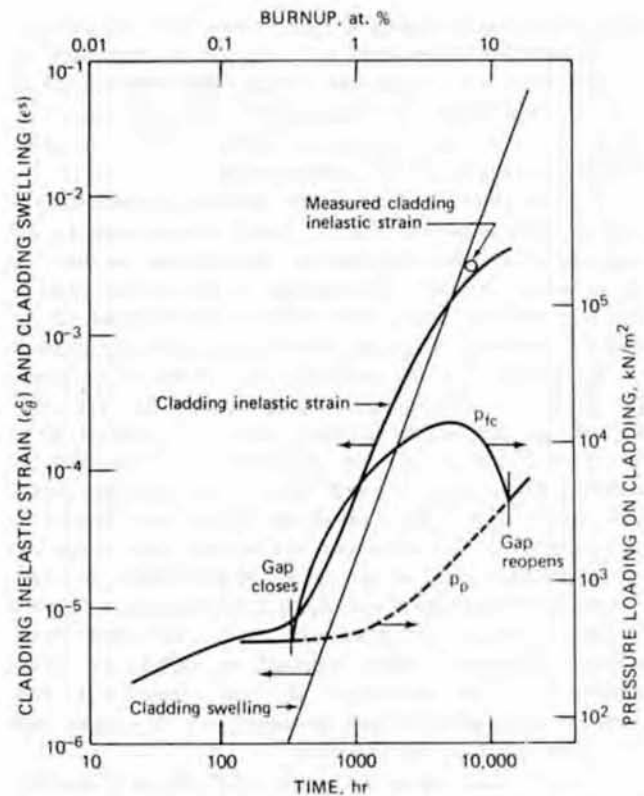

Fig. 21.8 Fuel-rod performance predicted by LIFE. Fuel density, 88.4% of theoretical density; fuel—cladding cold gap, 0.0066 cm; fuel-column length, 34 cm; fuel-pellet radius, 0.274 cm; cladding thickness, 0.038 cm; cladding temperature, 500°C; linear power, 440 W/cm; fast flux, 1.7×10^{15} neutrons cm^{-2} sec^{-1}. (After Ref. 14.)

with the single measurement. As a result of the recalibration, the predicted evolutions of strains and pressures with time shown in Fig. 21.8 are probably fairly reliable.

The inelastic strain in the cladding increases slowly from startup to ~400 hr into irradiation as a result of creep induced by thermal stresses produced by the temperature drop through the cladding. During this period, the fuel—cladding gap is open and the plenum pressure, which adds to the thermal stresses in the cladding, is low because not much fission gas has been released yet. At 400 hr the fuel has swollen sufficiently to contact the cladding, and the cladding becomes loaded by the fuel—cladding interfacial pressure rather than by the plenum pressure due to released fission gas. The sharp rise in the interfacial pressure following fuel—cladding contact causes a correspondingly steep increase in cladding inelastic strain. The fuel—cladding interfacial pressure reaches a maximum of ~12,000 kN/m² at ~5000 hr and thereafter decreases until the gap reopens at ~11,000 hr (although the actual fuel pin was not irradiated this long). Fuel—cladding contact is lost because cladding swelling [which increases as $(\Phi t)^n$ with $n > 1$] becomes more rapid than fuel swelling. The swelling curve for the cladding shown in Fig. 21.8 is one-third the volumetric void swelling and is similar in shape and magnitude to the swelling curve shown in Fig. 19.4. When the gap reopens, the cladding is once again loaded by the plenum-gas pressure, which has been increasing in an approximately linear fashion with time because of a roughly constant rate of fission-gas release from the fuel.

Figure 21.9 shows the computed effect of the initial fuel—cladding gap size, t_{gap}°, on the inelastic cladding strain. The smaller the cold gap, the sooner the fuel makes contact with the cladding and the larger are the resulting cladding strains. In the computations for the curves in this plot, the smeared density was held constant; thus an increase of the initial gap size must be accompanied by a decrease in the porosity of the fabricated fuel pellets (Eq. 21.1).

Figure 21.10 shows the effect of cladding temperature on the cladding permanent strain. The cladding-temperature variation at constant linear power was achieved by adjusting the sodium coolant inlet temperature in the code. Cladding strain at 375°C is low because the thermal creep rate, which is highly temperature sensitive (see Eq. 21.20b), is small. For the same stress the creep rate at 500°C should be much larger than that at 375°C; yet the curve for cladding strain at 500°C falls below that for 375°C cladding late in life. The explanation of this behavior is that 500°C is the peak swelling temperature for stainless steel (Fig. 19.3); so the cladding at this temperature literally runs away from the swelling fuel and prevents high interfacial pressure from developing. At temperatures above or below 500°C, the cladding does not possess this high recession velocity, and the strain due to fuel—cladding contact is more important than at 500°C. For cladding temperatures greater than 500°C, Fig. 21.10 shows that the cladding inelastic strains become large. At 600 and 700°C the creep strength of stainless steel is low, and the interfacial pressure is not relieved by cladding swelling, which virtually disappears at 600°C (Fig. 19.3). Consequently the combination of high temperature and high
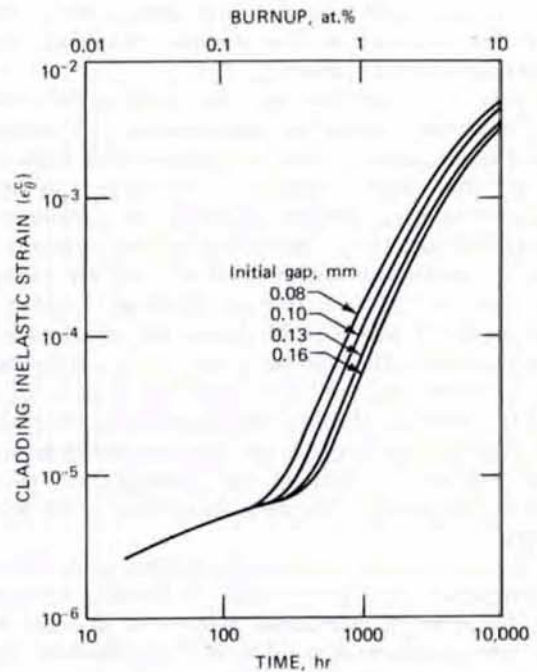
Fig. 21.9 Effect of fuel porosity and fuel—cladding gap size on fuel-element performance at constant smeared density. (After Ref. 14.)
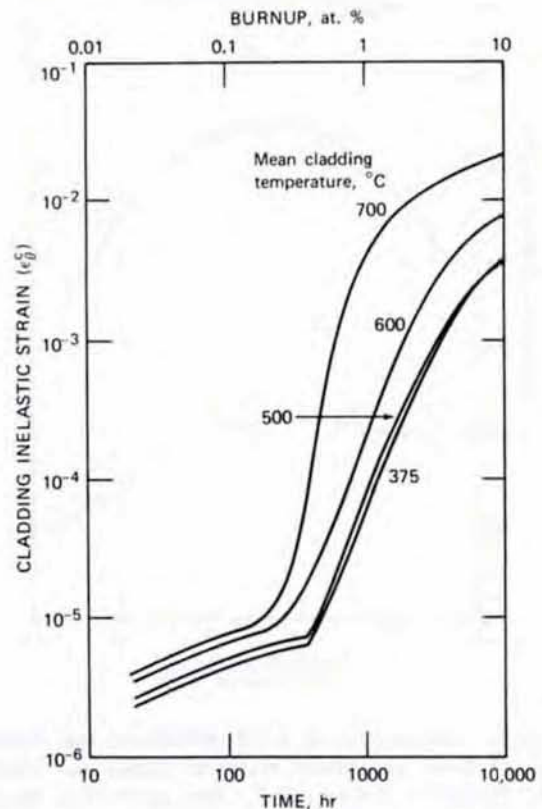

Fig. 21.10 Effect of cladding temperature on fuel-element performance for a fixed linear power of 440 W/cm. (After Ref. 14.)

stress in Eq. 21.20b generates large thermal-creep strains, which are manifest as the sizeable diametral strains predicted by the LIFE code.

Figure 21.10 predicts that the cladding deformation rate is drastically reduced at high burnups. This behavior is a direct consequence of the fission-gas swelling model used as a materials input function in the code. This model, although empirical, predicts saturation of swelling at all temperatures and more rapid attainment of saturation the higher the temperature. Such behavior is entirely consistent with such theoretical models of fission-gas swelling and release as BUBL and GRASS. In fact, the computation of fission-gas bubble distributions in Sec. 13.12 was performed for just such a saturated state of the fission gas in the fuel. When fuel swelling vanishes, the major reason for cladding deformation also disappears; the thermal stresses have been largely relieved by creep at high burnup, and the only remaining deformation process is that driven by the plenum pressure.

Figure 21.11 shows the axial distribution of the total cladding strain (i.e., $\epsilon_\theta^c + \epsilon^s$) and the swelling component alone for a set of irradiation parameters different from those used to prepare Figs. 21.8 to 21.10. However, it was again necessary to recalibrate LIFE by reducing fission-gas swelling to produce the agreement between code predictions and measurements shown in the graph. The relative importance of swelling strain, ϵ^s, and creep strain, ϵ_θ^c, is satisfactorily predicted by the program. The observed axial distribution of the total strain is sharper than that predicted by the code, but the trends are similar; inelastic strain is greatest at the midplane, where the flux and hence the linear power are the largest. The high-power center portion of the fuel pin swells more than the fuel near the ends of the rod; therefore the cladding at the midplane experiences a greater interfacial pressure than it does at other axial locations. The cladding creeps largely in response to the interfacial pressure, and hence the diametral strain is largest at the rod midplane.

Because the coolant sodium flows upward through the core, the swelling strain is not symmetric about the core midplane. Cladding swelling due to void formation is greatest slightly above the midplane and decreases rapidly further up the core because the cladding temperature exceeds the maximum for swelling while the flux is decreasing. In the lower half of the core, however, the cladding temperature is generally closer to the 500°C maximum swelling temperature than it is in the top half of the core. Hence the swelling strain does not drop off as rapidly when moving from the midplane to the bottom of the fuel rod as it does when moving in the opposite direction (see problem 21.7 at end of the chapter).

21.4.2 Axial Ratchetting

If the linear power of a fuel rod is subject to continuous off/on cycling and if fuel—cladding contact is made at a power less than the maximum, permanent axial deformation of the cladding may occur during each cycle. This mode of permanent strain of the cladding, which is fundamentally different from the steady deformations considered earlier in this chapter, is termed *axial ratchetting*. It has been studied analytically, but the phenomenon is difficult to observe because of the narrow range of conditions that permit its operation (Refs. 8, 10, 13, 15).

The process of axial ratchetting is shown schematically in Fig. 21.12. At zero power there is a fuel—cladding gap (Fig. 21.12a). As the rod power is raised, the fuel, which is hotter than the cladding, expands more than the cladding both axially and radially and fuel—cladding contact occurs before the maximum power in the cycle is achieved (Fig. 21.12b). The interaction forces between these two members place the cladding in tension both axially and tangentially, and the fuel experiences compression. Continued expansion of the nearly incompressible fuel further increases the tensile stresses in the cladding. When the yield point of the cladding is exceeded, immediate plastic flow occurs. If the maximum power is maintained long enough, the cladding creeps under the influence of the tensile stresses. For cladding deformation in the z-direction to occur, there must be significant friction between the fuel and the cladding; otherwise the fuel simply slips upward without taking the cladding along with it.

Fig. 21.11 Comparison of LIFE predictions and measurements of total permanent diametral strain and swelling strain. (From A. Boltax, W. E. Ray, and W. J. Rowan, Oxide Fuel Element Development Quarterly Progress Report of the Period Ending September 30, 1972, USAEC Report WARD-3045-T-3-9, Westinghouse Electric Corp., January 1973.)

$\mathscr{P}=0$ $\mathscr{P}^*$ $\mathscr{P}_{max}$ $\mathscr{P}=0$ $\mathscr{P}^*$
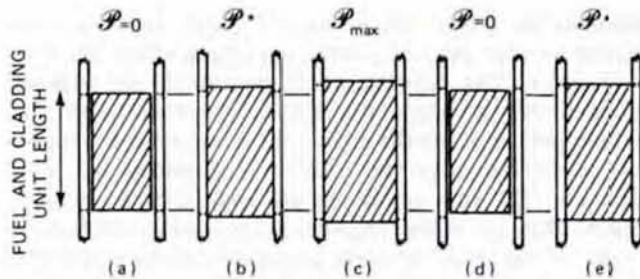
(a) (b) (c) (d) (e)

Fig. 21.12 Diagram of the axial ratchetting mechanism. The marks in the cladding provide reference points from which deformations can be measured. The lines between each drawing show the original position of the reference points. (After Ref. 8.) $\mathscr{P}^*$, linear power at which fuel—cladding contact occurs; $\mathscr{P}_{max}$, maximum linear power in cycle.

At the end of the maximum-power stage (Fig. 21.12c), permanent axial deformation of the cladding has occurred. When the power is reduced, the fuel returns to nearly its original size, but the cladding, having been deformed irreversibly, does not (Fig. 21.12d). Only the elastic strain of the cladding is recovered when contact with the fuel is lost. When the power cycle is repeated, fuel—cladding contact is again made, and the cladding receives another increment of permanent deformation (Fig. 21.12e). If the fuel piece returns to precisely the same shape and volume at the zero-power part of each cycle and thermally expands by exactly the same amount at each power increase, cladding deformation will cease after a number of cycles sufficient to extend the tube plastically to a size which either does not provide sufficient friction for the contact or which no longer results in creep or plastic flow during contact. However, two mechanisms are capable of continuing the axial ratchetting process indefinitely:

1. The fuel may consolidate during the power-reduction period in such a way that the fuel—cladding gap tends to fill up with fuel originating from the main body of the fuel stack. Fuel movement into the reopened gap may occur by gravity (i.e., by cracked pieces falling from the fuel and becoming lodged in the gap).

2. If the fuel is swelling at a constant rate during power cycling (e.g., by solid-fission-product swelling), the fuel volume at the end of each cycle continually increases. Fuel—cladding contact is thus made easier, and the fuel may be capable of pumping the cladding and of continuing indefinitely to deform the cladding during each cycle. Figure 21.13 shows the results of calculations with the cladding behavior code CRASH[8] for a situation in which both axial and radial ratchetting set in during uniform power cycling of a fuel rod.

21.4.3 Bambooing

Another fuel-rod deformation problem that, to a first approximation, can be treated by linear thermoelasticity theory is the calculation of the strain in a finite cylinder (i.e., a fuel pellet) due to application of a radial temperature gradient. As a result of the absence of restraint at

the top and bottom of the pellet, the ends experience greater radial strain than the central cross section. The hourglass shape assumed by the pellets produces greater fuel—cladding interaction at the pellet—pellet interfaces than at axial positions corresponding to the middle of the pellets. The cladding deforms in response to this non-uniform interaction with the fuel by developing circumferential ridges. The phenomenon is known as *bambooing* and is shown schematically in Fig. 21.14. The shapes of the pellets can be computed from thermoelasticity theory if the interaction of a pellet with its neighbors and with the cladding is neglected (i.e., if a single free pellet is considered). In this approximation the upper and lower faces of the pellet can be characterized by plane stress and the cross section through the middle by plane strain. The thermoelastic solution is discussed by Matthews.[9]

Bambooing is possible only before the pellets have sintered together and formed a continuous fuel stack. The phenomenon is most likely to occur in fuel elements immersed in a coolant at sufficiently high pressure to collapse the cladding onto the fuel, which is the case in pressurized-water reactor fuels.

21.5 VOID SWELLING EFFECTS ON OTHER CORE COMPONENTS

The analysis in the first four sections of this chapter was directed at determining the longevity of a single fuel element in an LMFBR. Implicit in this discussion was the assumption that the lifetime of the reactor core was dictated by the time at which unacceptable numbers of cladding ruptures began to occur. However, fuel elements are bundled together and inserted into *wrappers* or *ducts*, which are packed together to form the core. Primarily because of void swelling, core lifetime may be limited by undesirable irradiation-induced deformations of the wrapper tube and not by the failure of fuel-element cladding. The consequences of void swelling in core
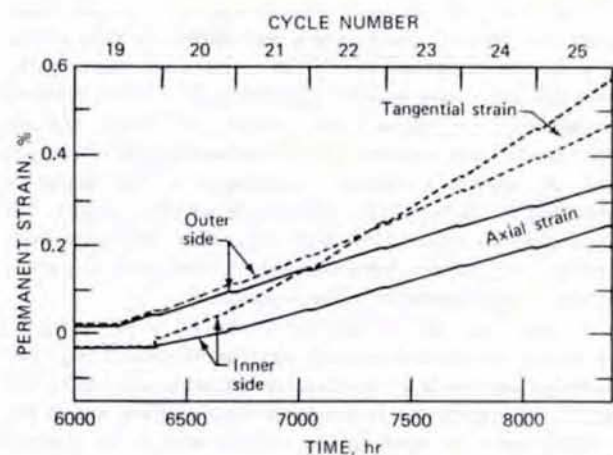

Fig. 21.13 Code predictions of axial and radial strains of cladding during ratchetting induced by power cycling. Fuel—cladding contact first occurs during the 19th cycle. (After Ref. 8.)
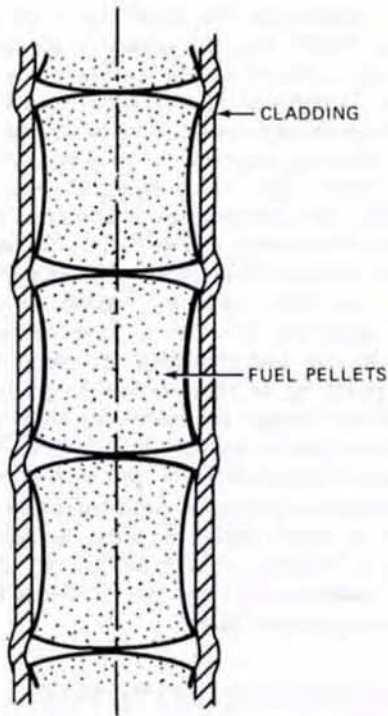
Fig. 21.14 Bambooing of fuel elements.

components other than fuel elements on LMFBR core performance have been reviewed by Huebotter and co-workers,[16-18] and much of the discussion in this section is based on their analyses.

Figure 21.15 shows longitudinal and cross-sectional views of an LMFBR *fuel assembly*. A cutaway rendering of the same component is shown in Fig. 10.4. There are 217 fuel elements placed inside the hexagonal-shaped wrapper in the triangular pattern shown in the cross-sectional view. Wires wrapped around each fuel element (Fig. 10.2) act as spacers and provide passageways for sodium flow past each element in the bundle. The wrapper is approximately 0.35 cm thick except for areas at the top and just above the core where the walls are thickened by ~0.06 cm to form *spacer pads*. These are the zones where neighboring assemblies interact mechanically. Excessive void swelling at these contact points could cause stresses in the duct walls high enough to result in assembly failure, especially if the metal is embrittled by helium. The spacer pads are placed above the core region to escape the high flux that promotes both swelling and helium embrittlement of steel and thus avoid fracture at interassembly contact points.

A nozzle is attached to the bottom end of the wrapper. The nozzle is inserted into the permanent structure in the bottom of the reactor vessel and so supports the entire fuel assembly in cantilever fashion. Coolant sodium enters the assembly through slots in the nozzle and flows upward around the fuel bundle inside the wrapper.

Figure 21.16 shows two neighboring fuel assemblies supported by insertion of their nozzles in the upper and lower *grid plates*, which are fabricated from stainless steel. These plates are ~3 m in diameter and ~10 cm thick. The

holes in the upper and lower grid plates are accurately aligned so that the fuel assembly is plumb when seated in both plates. The *handling heads* on top of the wrapper tubes permit a refueling machine operating under the sodium pool in which the entire core is immersed to remove fuel assemblies after the allotted fuel burnup has been achieved. The fuel assemblies are approximately 4 m in length. They are packed together in the honeycomb fashion shown in Fig. 21.17 to form an approximately hexagonal-shaped core that contains about 400 fuel assemblies and is of the order of 3 m across the flats (for a 1000-MW reactor). Approximately one-tenth as many *guide tubes* for safety and control rods as there are fuel assemblies are interspersed among the fuel assemblies. Two rows of blanket assemblies (containing rods filled with $^{238}UO_2$) comprise the periphery of the core.

The principal functions of the hexagonal wrapper around each fuel- or blanket-element bundle are:

1. To prevent the sodium coolant from bypassing the high-flow-resistance path alongside the fuel-pin bundle and flowing up the interassembly gap instead.

2. To provide structural support for the bundle of fuel elements or control rods contained in the wrapper.

3. To provide mechanical means (by the handling heads) for removal of spent fuel and replacement with fresh fuel.

4. To provide a barrier against propagation to the rest of the core of an accident that might be caused by rupture of one or more fuel pins in an assembly.

Other components of the core are:

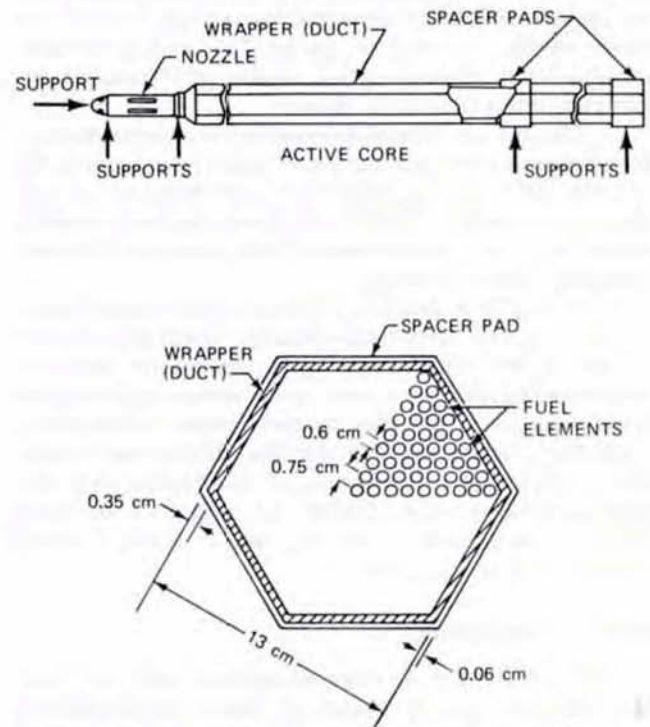1. Grid plates that support the assemblies.

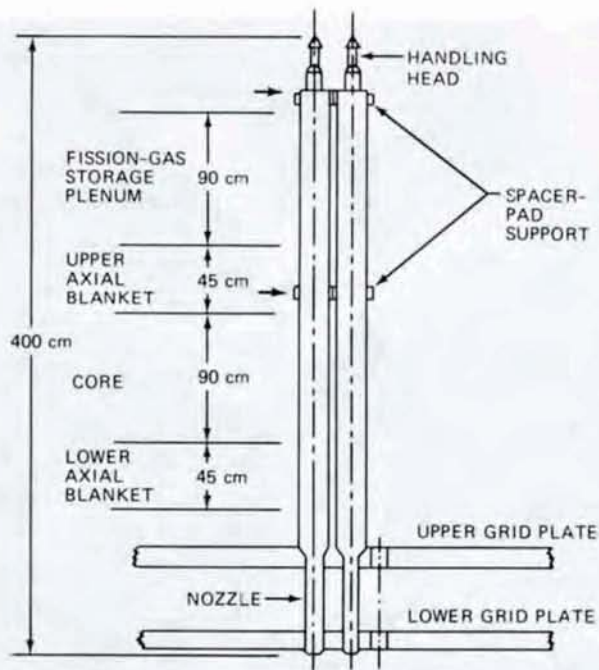Fig. 21.15 Typical fuel assembly of an LMFBR. (After Refs. 16 to 18.)

Fig. 21.16 Mounting of fuel assemblies on the grid plates. (After Ref. 17.)
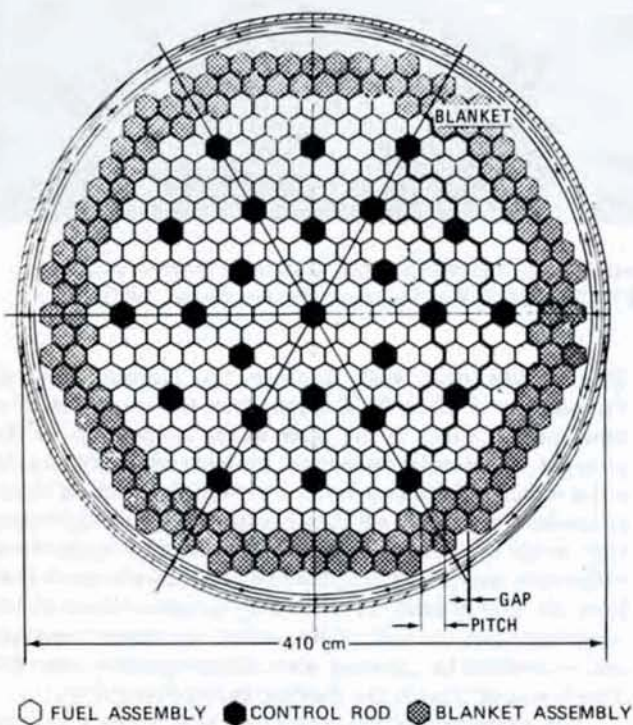

○ FUEL ASSEMBLY ● CONTROL ROD ⊛ BLANKET ASSEMBLY

Fig. 21.17 Arrangement of assemblies in the reactor core. [From B. J. Goulding, 1000-MW(e) LMFBR Accident Analysis and Safety Design Study. Topical Report, Effect of Irradiation-Induced Metal Swelling on the Reference Design, USAEC Report BAW-1355, Babcock & Wilcox Co., November 1970.]

2. An instrument plate located above the core in the sodium pool. This component supports thermocouples and flowmeters for monitoring the sodium outlet conditions.

3. A core-restraint component that is designed to exert a lateral force on the array of assemblies to correct the disarray of the core due to bowing of the assemblies.

A prototype core-restraint device, a *core clamp*, is shown in Fig. 21.18. This component consists of six hydraulically operated yokes or rams that press inward on the six sides of the core which consist of the blanket assemblies (Fig. 21.17). The clamp acts at the elevation of the spacer pads on the assemblies. The object of the core clamp is:

1. To provide a calculable and reproducible structural response of the core which, if left unrestrained, would be substantially disarrayed by swelling and bowing of the wrappers.

2. To maintain the tops of the assemblies in position so that the handling heads can be located and grappled by the refueling machine, which operates under opaque sodium.

3. To provide adequate clearance and maintain sufficient duct straightness so that assemblies can be removed or inserted from the array without undue vertical friction forces due to rubbing against neighboring assemblies. The core clamp is released for refueling operations.

The hydraulically actuated core clamp shown in Fig. 21.18 is used only to test the mechanical performance of mock-up LMFBR cores; actual fast breeder reactors (in the United States at least) will use a passive restraint system in which core motion is restrained by a fairly rigid barrel-shaped structure enclosing it.

Concern with these aspects of overall core structural performance (and indeed, the reason for the decision to use core restraint) is a direct consequence of swelling of steel by voids generated under fast-neutron bombardment. The earlier sections of this chapter considered the effect of void swelling on the performance of individual fuel elements. In this instance it was found that metal swelling may be beneficial to fuel-element performance because it acts to relieve the fuel—cladding interfacial pressure built up by fuel swelling. When the other core components swell, however, there is no such redeeming feature; the consequences are uniformly undesirable. The problem is limited to the assembly wrapper tube because the other components of the core (grid plates, instrument plates, and core clamp) are in regions of sufficiently low flux that the effect of swelling on them is not significant even over the ~30-year lifetime of the reactor plant.

The effects of void swelling on the assembly may be divided into the uniform volume increase of metal (axial and radial) and the differential swelling caused by non-uniform temperature and flux between the side of an assembly closest to and the side furthest away from the core axis.

21.5.1 Elongation

Elongation refers to the permanent axial extension of an assembly due to void swelling. The axial-swelling strain may be computed by integrating one of the void-swelling
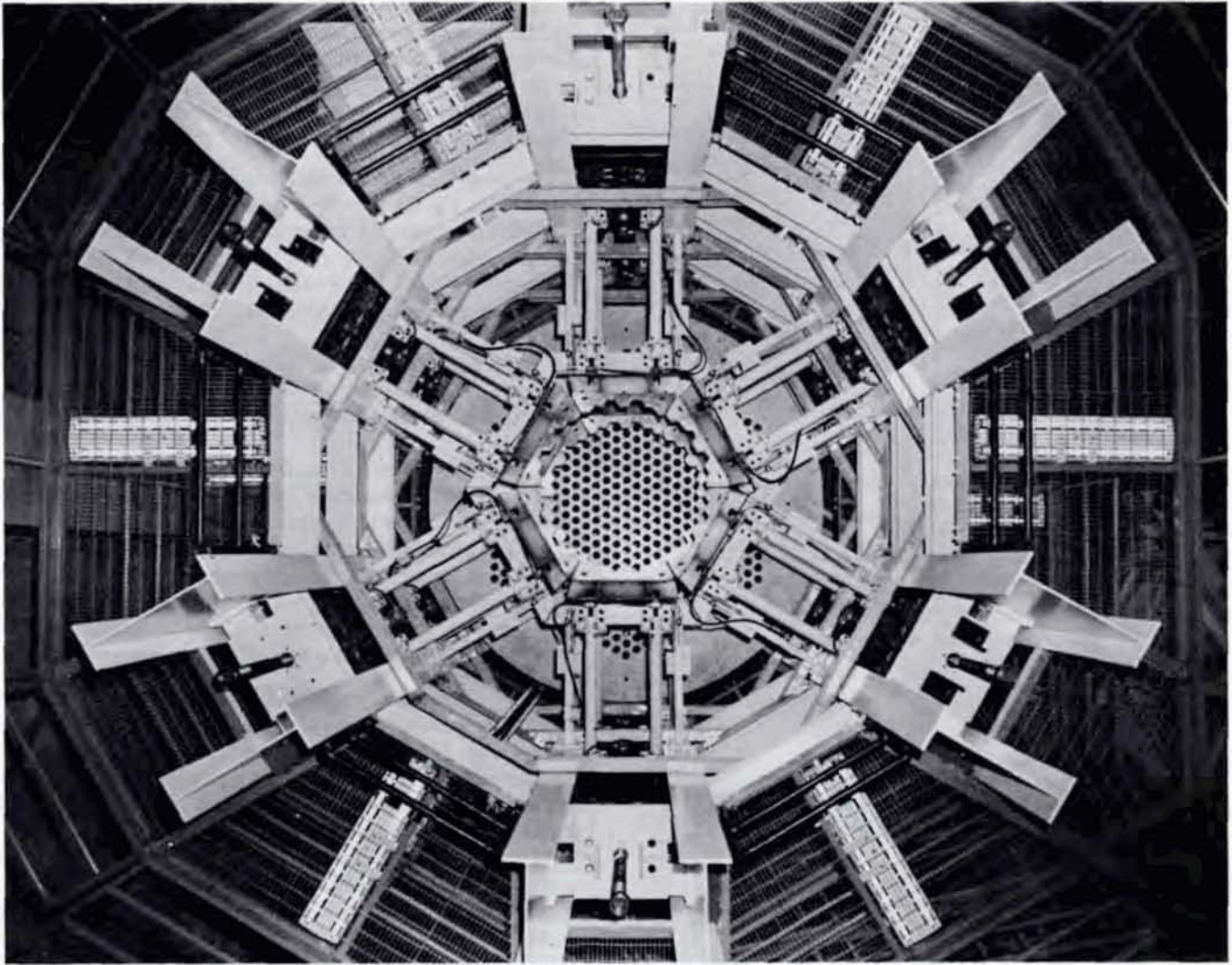
Fig. 21.18 A prototype core clamp. (From J. W. French, Core Restraint Developments, Quarterly Progress Report for Period Ending November 30, 1973, USAEC Report WARD-CR-3045-4, Westinghouse Electric Corp., 1973).

equations presented in Chap. 19 (e.g., Eq. 19.12b) over the length of the assembly, taking into account the axial variation of both the fast-neutron flux (which is approximately cosine in shape) and the coolant temperature (which increases monotonically from inlet to outlet). The axial strain or elongation is one-third the volume swelling so computed. Figure 21.19 shows the results of such a calculation for the rings of assemblies at different radial distances from the core axis. The walls of the duct closest to the core center elongate more than the opposite walls because of the radial flux and temperature gradients (these gradients are also responsible for bowing, which is discussed in the next section). The central fuel assembly elongates more than 4 cm, which corresponds to an axial swelling strain of about 1%. Elongation of the assemblies by this amount complicates the design of the machine for handling the assemblies, but this problem does not appear to be insurmountable.

Void swelling also causes the fuel elements proper to grow in length. The growth of the cladding is greater than

that of the duct walls because the cladding midwall temperature is 50 to 75°C higher than the average sodium temperature, which is the same as the temperature of the wrapper. A potential mechanical problem arises because the wires wrapped in helical fashion around the cladding to act as spacers (Fig. 10.2) are closer to the sodium temperature than to the cladding midwall temperature. This temperature difference means that the cladding swells axially more than does the wire around it (by ~0.2%). Excessive stress on the wire wrap near the end of life, which may cause breakage, can be avoided by allowing some initial slackness when the wire is wound around the cladding during fabrication.

The neutronics of the reactor are affected by core axial growth. The estimated reactivity decrease due to the elongation is $2.* This loss must be compensated for by increasing the mass of fissile plutonium in the fresh fuel,

---

*A dollar ($) is equal to a reactivity of one delayed-neutron fraction (~0.00023 for plutonium).
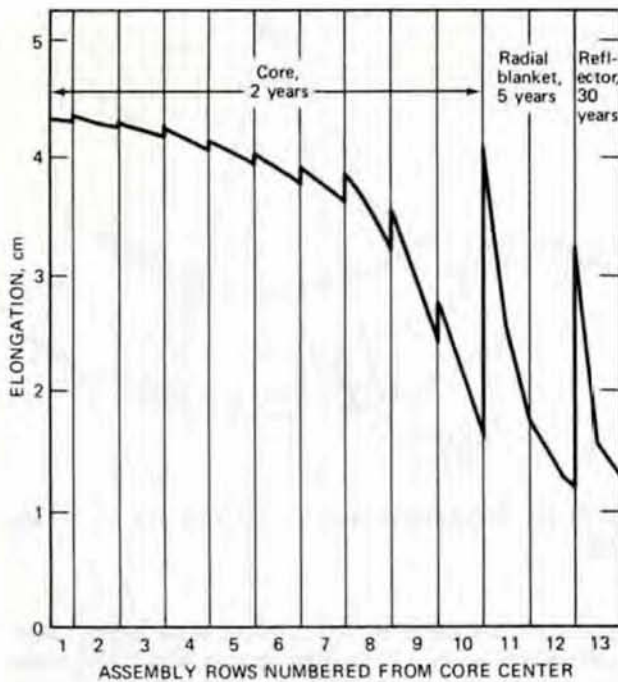
Fig. 21.19 Elongation of wrapper walls due to void swelling at the end of the nominal lifetime of each component. (After Ref. 18.)

which represents the first but by no means the worst adverse economic consequence of void swelling.

21.5.2 Dilation

Dilation refers to the uniform radial growth of the core due to swelling of each of its component assemblies. Radial dilation of these components is computed by the method described for calculating elongation. Figure 21.20 shows the radial dilation of the wrappers in various rings of the core after ∼2 years of operation. Maximum dilation occurs just above the core midplane because this location offers the combination of flux and temperature most propitious to void swelling (see problem 21.7 at end of chapter). At this position the diametral expansion of the central assembly is ∼0.6 cm. The consequence of radial dilation of the wrappers is the reduction in the clearance between assemblies. If swelling were absent, a gap between neighboring assemblies of ∼1.3 mm would be sufficient for assembly removal and insertion. However, as a result of void swelling, the central assembly must be separated from its six neighbors by gaps of ∼7 mm. The required clearance is reduced as the periphery of the core is approached. If initial clearances, ultimately to be filled by the swelling wrappers, were not provided, the core would push outward radially during irradiation and very quickly would cause unacceptable misalignment of control rods and their above-core extensions and handling heads and the refueling machine. The larger than normal gap size between the assemblies in the core introduces a significant economic penalty because the gap is filled with sodium, not fuel. The large clearances reduce the fuel-to-metal ratio of the core,

thereby increasing the critical mass and decreasing the breeding ratio.

The bundle of fuel rods inside the assembly swell radially more than the duct wall, and sufficient clearance must be provided during fabrication to accommodate differential swelling of fuel pins and wrapper. The ∼1.5% clearance needed for this purpose is more than the nominal clearance needed to load the bundle into the assembly. The loose fit of the fuel-pin bundle early in irradiation does not appear to cause operational problems.
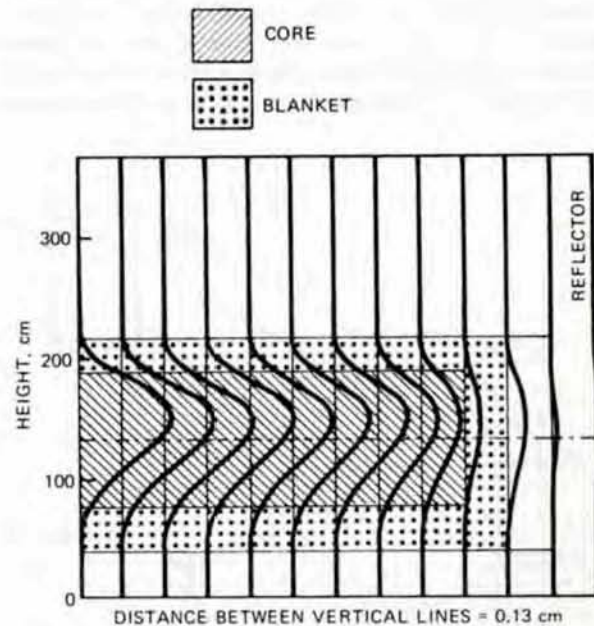

Fig. 21.20 Dilatation of wrapper walls due to void swelling at end of life. (After Ref. 18.)

21.6 FUEL-ASSEMBLY BOWING

Bowing refers to the loss of duct straightness caused by differential temperatures and swelling strains on opposite faces of an assembly. This consequence of swelling is more severe than the effect of uniform expansion just discussed, which at least can be computed with reasonable accuracy. Bowing, on the other hand, involves a complex combination of thermal expansion, void swelling, irradiation creep, and mechanical interaction between neighboring assemblies which do not deform by equal amounts and which exert forces on each other at the spacer pads. Several computer programs are available for numerical analysis of the bowing problem. The codes CRASIB[19] and AXICRP[20] subdivide the fuel assembly into regions (similar to the method used in fuel-element modeling codes) and calculate the time-dependent loads, stresses, and shapes of the ducts due to nonuniform thermal expansion coupled with void swelling and irradiation creep. The fuel pins inside the wrapper are very compliant compared to the thick-walled duct and are not considered in the calculation. The fuel pins are assumed to follow the bowing of the duct. These codes, however, do

not allow for interassembly mechanical interaction. This aspect of bowing is treated in detail in the BOW-V code[21] which, unfortunately, is restricted only to thermal bowing. Complete structural analysis of the entire array of assemblies requires mating of CRASIB and BOW-V. We review here some of the elementary notions that underlie the computational methods used in these codes.

21.6.1 Elementary Beam Theory

Figure 21.21 shows a beam with its long dimension in the z-direction. The cross section may be any shape that is symmetric about the x- and y-axes, but a rectangle of dimensions 2h and b has been chosen for the present discussion. Bending occurs in the x–z plane because of (1) forces applied on the upper or lower faces of the beam in
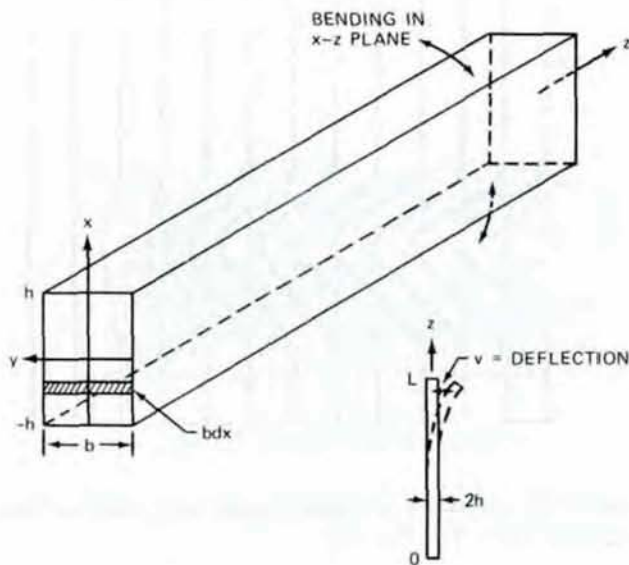
Fig. 21.21 Bending of a beam.

the x-direction and (2) volumetric thermal and swelling strains that depend on x. These strains are assumed to be symmetric about x = 0 and to vary linearly from x = −h to x = h.

The beam bends in the x–z plane as a result of one or a combination of these effects. To determine the stress distribution and the lateral displacement v(z) of the beam, we must satisfy three basic relations: (1) the strain–displacement equation, (2) the equilibrium equations, and (3) the constitutive equation. Solution of these equations requires specification of appropriate boundary conditions on the beam.

21.6.2 The Strain–Displacement Relation

The geometry of the curved beam at a particular z-position is shown in Fig. 21.22. The radius of curvature of the central plane (x = 0) is denoted by ρ. This plane is called the neutral fiber because it experiences zero strain compared to the neighboring fibers, and the length of a
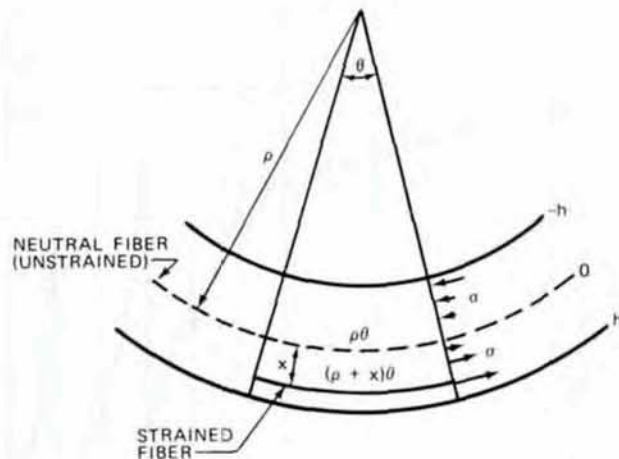

Fig. 21.22 Longitudinal section (x–z plane) of a bent beam.

segment on this plane remains constant as the beam is bent. However, the length of the fiber at $\rho + x$ is $(\rho + x)\theta$, which is greater than the length before bending by an amount $x\theta$. Therefore the strain in the z-direction of the fiber at position x is

$$\epsilon_z = \frac{x\theta}{\rho\theta} = \frac{x}{\rho}$$

A theorem of plane geometry states that the reciprocal of the radius of curvature (provided that ρ is large) is equal to the second derivative of the curved segment. Denoting the deflection of the beam away from the z-axis in the x–z plane by v (see inset of Fig. 21.21), we have

$$\frac{1}{\rho} = \frac{d^2 v}{dz^2}$$

Combining the above two relations, we obtain the axial strain–displacement equation

$$\epsilon_z = x\frac{d^2 v}{dz^2} \tag{21.57}$$

21.6.3 Equilibrium Conditions

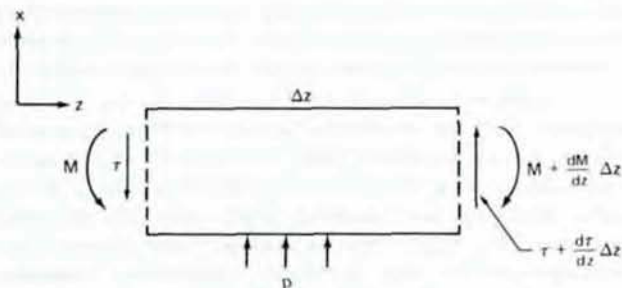Figure 21.23 shows the forces and moments acting on a slice of beam of thickness Δz. The sides of the beam are

Fig. 21.23 Forces and moments on a section of a beam.

subject to an applied load (normal stress) distribution denoted by p(z). The cross section perpendicular to the z-axis experiences a shear force denoted by τ and a bending moment about the y-axis due to the distribution of normal stresses shown in Fig. 21.22. The moment acting on the differential area bdx is the product of the force σbdx and the lever arm x, or dM = xσbdx. Integrating over the entire cross section yields the moment due to the stress distribution

$$M = b \int_{-h}^{h} x\sigma \, dx \qquad (21.58)$$

In order that the net force in the x-direction on the element in Fig. 21.23 be zero, we must have

$$\frac{d\tau}{dz} = -p \qquad (21.59)$$

and, for the body to be in rotational equilibrium, the resultant torque must be zero

$$\frac{dM}{dz} = \tau \qquad (21.60)$$

Eliminating τ between the above two equations yields

$$\frac{d^2 M}{dz^2} + p = 0 \qquad (21.61)$$

which is the desired equilibrium relation for the beam.

21.6.4 Constitutive Relation

The strain in the z-direction, ϵ_z, is the sum of the elastic strain due to the internal stress distribution, thermal expansion, swelling, and creep. Neglecting creep (we will return to it later), the axial strain is

$$\epsilon_z = \frac{\sigma}{E} + \alpha T + \epsilon^s \qquad (21.62)$$

where E is the Young's modulus, and α is the linear coefficient of thermal expansion. The temperature T is measured with respect to the vertical (y—z) plane bisecting the beam, and ϵ^s is one-third the volume swelling due to voids in the metal. Replacing the left-hand side of Eq. 21.62 by the strain—displacement relation (Eq. 21.57), multiplying the resulting equation by xbdx, and integrating over the x-dimension yields

$$\frac{d^2 v}{dz^2} b \int_{-h}^{h} x^2 \, dx = \frac{1}{E} b \int_{-h}^{h} x\sigma \, dx$$

$$+ \alpha b \int_{-h}^{h} Tx \, dx + b \int_{-h}^{h} \epsilon^s x \, dx$$

We assume a linear variation of temperature across the beam (the x-axis corresponds to the negative of the radial direction from the core center line)

$$T = \frac{\Delta T}{2h} x \qquad (21.63)$$

where ΔT is the temperature difference between the hot and cold sides of the beam. Similarly the swelling strain is assumed to vary linearly in x

$$\epsilon^s = \frac{\Delta \epsilon^s}{2h} x \qquad (21.64)$$

where $\Delta \epsilon^s$ is the difference in swelling strain between the flats of the assembly closest to and furthest from the core center line and is a function of the radial flux and the temperature distribution in the core. It also varies with time, whereas the temperature difference across the flats, ΔT, does not.

The moment of inertia of the rectangular beam about the y-axis is defined by

$$I = b \int_{-h}^{h} x^2 \, dx \qquad (21.65)$$

The moment of inertia is a geometrical property of the beam cross section. Equation 21.65 applies to the solid rectangular beam, but similar formulas may be obtained for other shapes, such as the hollow hexagonal configuration of the wrapper of a fuel assembly. Using Eqs. 21.63 to 21.65 and the definition of the moment, Eq. 21.58, the beam-deflection differential equation becomes

$$\frac{d^2 v}{dz^2} = \frac{M}{EI} + \frac{\alpha \, \Delta T}{2h} + \frac{\Delta \epsilon^s}{2h} \qquad (21.66)$$

Determination of the deflection profile or camber of the beam requires specification of the moment M and integration of Eq. 21.66 with appropriate boundary conditions.

The total deflection v consists of contributions from the applied load (first term on the right-hand side) and from thermal and swelling expansions. Since the total deflection can be obtained by adding these three contributions, we examine each one separately.

1. Consider the assembly shown in Fig. 21.16 inserted into the grid plates by its nozzle. Let z = 0 be the axial location of the upper grid plate, and suppose that a force F is applied laterally to the top spacer pad, which is a distance L from the upper grid plate. Since the applied load is zero except at x = L, Eq. 21.61 can be integrated to yield

$$M = az + b$$

where the constants a and b are determined by conditions applied at the free end. The applied force F is represented as a shear stress τ on the end of the member. In addition, the moment M must vanish at the free end. The appropriate boundary conditions at z = L are

$$M = 0$$
$$\tau = F$$

Because the load p is zero along the length of the beam, Eq. 21.59 shows that τ is constant along the length of the beam or that $\tau = F$ for all z. Equation 21.60 requires that dM/dz = F, which specifies one of the integration constants as a = F. The second integration constant follows from the condition of zero moment at z = L; the moment in the beam is thus

$$M = -F(L - z) \qquad (21.67)$$

Since the assembly is cantilevered from the grid plate, we can write

$$v(0) = \left(\frac{dv}{dz}\right)_0 = 0 \qquad (21.68)$$

Substituting Eq. 21.67 into 21.66 (neglecting the last two terms on the right-hand side), integrating, and using the boundary conditions at z = 0 given by Eq. 21.68, we find the deflection

$$v = -\frac{Fz^2}{2EI}\left(L - \frac{z}{3}\right) \qquad (21.69)$$

2. For a linear temperature distribution along the x-direction of the assembly wrapper, the temperature distribution through the beam is given by Eq. 21.63. In the absence of applied loads and void swelling, the deflection due to the nonuniform temperature across the assembly is obtained by solution of

$$\frac{d^2v}{dz^2} = \frac{\alpha\Delta T}{2h} \qquad (21.70)$$

The temperature difference across the flats, ΔT, is a function of height z and is computed from thermal analysis of the fuel assembly. For the special (but unrealistic) case of ΔT independent of z, integration of Eq. 21.70 with the boundary conditions of Eq. 21.68 yields

$$v = \frac{\alpha\Delta T}{4h}z^2 \qquad (21.71)$$

3. For the transverse linear swelling profile, the deflection is obtained from

$$\frac{d^2v}{dz^2} = \frac{\Delta\epsilon^s}{2h} \qquad (21.72)$$

which requires specification of the axial variation of $\Delta\epsilon^s$ and appropriate boundary conditions for integration.

In the absence of creep (either thermal or irradiation), unrestrained deflection of a fuel assembly with both temperature and swelling gradients is obtained by solving Eqs. 21.70 and 21.72 independently, each subject to Eq. 21.68. The total deflection profile is obtained by adding (superposing) the two component deflections. The result of such a calculation is shown in Fig. 21.24. The combined thermal and swelling deflections amount to 6 cm at the top of the fuel assembly. The thermal component of the bowing is recovered when the reactor is shut down for refueling, but the permanent camber due to swelling remains. This graph illustrates the potential difficulty of locating the handling heads of the assembly under sodium and the virtual certainty of mechanical interaction between assemblies in adjacent rows. Lateral forces, due either to the natural interaction of nearby assemblies or to the compacting action of the core restraint, are generally applied at the spacer-pad elevations. The deflections induced by these mechanical loads must be added to those arising from unrestrained bowing. The mechanical forces may be applied at more than one axial position, and the moment distribution is generally more complex than that given by Eq. 21.67. If the loads are due to interaction of adjacent assemblies at a single axial position, the force F in Eq. 21.67 is not known a priori but must be determined in the course of solving the deflection equation for all interacting assemblies (see problem 21.8 at the end of the chapter).
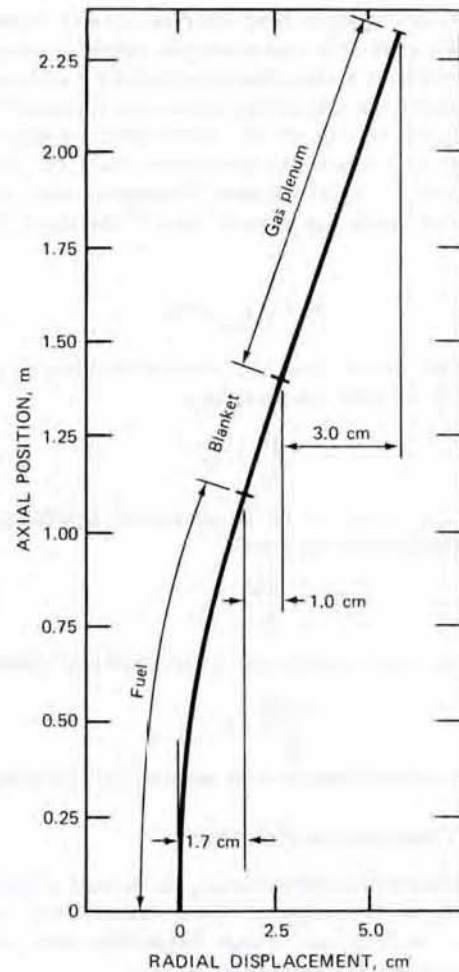

Fig. 21.24 Free bowing of a fuel assembly due to nonuniform thermal expansion and void swelling. (After Ref. 18.)

21.6.5 Effect of Irradiation Creep on Bowing

The major deficiency of the analysis just presented is the exclusion of creep, which acts to relieve the stresses established by the combined effects of the transverse temperature and swelling distributions and the mechanical interaction between assemblies. Because of the relatively low temperature of the duct walls (<650°C), thermal creep is not as important as irradiation creep. Irradiation creep is especially effective in the high-flux core region. To illustrate the effect of irradiation creep on bowing, we take the simple irradiation-creep expression (the steady-state creep component in Eq. 19.176)

$$\dot{\epsilon}^c = C\Phi\sigma \qquad (21.73)$$

Relief of the bending stresses in the duct by irradiation creep is a form of stress relaxation. This phenomenon may be most clearly explained by considering a bar of solid loaded in tension in which creep takes place at a rate given by Eq. 21.73. Suppose the bar is subject to an initial tensile stress σ_0 that causes an initial elastic strain equal to σ_0/E.

We now assume that the initial strain is held constant. The stress is reduced with time by creep of the material in a manner such that the total strain σ_0/E does not change. Thus the stress at any time during the test is given by

$$\frac{\sigma}{E} + \epsilon^c = \frac{\sigma_0}{E} \qquad (21.74)$$

where ϵ^c is the creep strain. Differentiating this equation with respect to time yields

$$\frac{1}{E}\frac{d\sigma}{dt} = -\dot\epsilon^c = -C\Phi\sigma \qquad (21.75)$$

Integration gives the stress-relaxation formula for this simple case as

$$\sigma = \sigma_0 \exp(-CE\Phi t) \qquad (21.76)$$

The stress at constant strain is seen to decrease exponentially with time.

To introduce creep into the beam-deflection problem wherein applied forces, nonuniform thermal expansion, and nonuniform swelling are also present, we express the constitutive equation by

$$\epsilon_z = x \frac{d^2 v}{dz^2} = \frac{\sigma}{E} + \alpha T + \epsilon^s + \epsilon^c \qquad (21.77)$$

which may be recognized as the constitutive equation for the metal (Eq. 21.9 for uniaxial tension or compression). The term σ/E on the right-hand side of Eq. 21.77 arises from the applied lateral load on the member. Multiplying Eq. 21.77 by bxdx and integrating from $x = -h$ to $x = h$ yields

$$I \frac{d^2 v}{dz^2} = \frac{M}{E} + b \int_{-h}^{h} (\alpha T + \epsilon^s) x\, dx + b \int_{-h}^{h} \epsilon^c x\, dx$$

where Eqs. 21.58 and 21.65 have been used. Assuming that the applied load creates a bending moment given by Eq. 21.67 and that the temperature and swelling gradients are constant (Eqs. 21.63 and 21.64), we find the above equation becomes

$$\frac{d^2 v}{dz^2} = -\frac{F(L-z)}{EI} + \frac{\alpha\,\Delta T}{2h} + \frac{\Delta\epsilon^s}{2h} + \frac{b}{I}\int_{-h}^{h} \epsilon^c x\, dx \qquad (21.78)$$

According to Eq. 21.73, the creep strain is

$$\epsilon^c = C\Phi \int_0^t \sigma\, dt'$$

and the integral in Eq. 21.78 can be written as

$$\frac{b}{I}\int_{-h}^{h} \epsilon^c x\, dx = \frac{bC\Phi}{I}\int_{-h}^{h} x\, dx \int_0^t \sigma\, dt'$$

$$= \frac{C\Phi}{I}\int_0^t \left(b\int_{-h}^{h} x\sigma\, dx \right) dt'$$

The second equality was obtained by interchanging the order of integration. Equation 21.58 shows that the quantity in parentheses is equal to the moment M, which is given by Eq. 21.67. Making the appropriate substitutions yields

$$\frac{b}{I}\int_{-h}^{h} \epsilon^c x\, dx = -\frac{C\Phi(L-z)}{I}\int_0^t F(t')\, dt'$$

and the deflection equation, Eq. 21.78, becomes

$$\frac{d^2 v}{dz^2} = -\frac{L-z}{EI}\left[F(t) + C\Phi E \int_0^t F(t')\, dt' \right]$$
$$+ \frac{\alpha\,\Delta T}{2h} + \frac{\Delta\epsilon^s}{2h} \qquad (21.79)$$

Because of creep, F is a function of time.

To illustrate the nature of the solution of Eq. 21.79, we take the simple case in which the boundary conditions are given by Eq. 21.68 and ΔT and $\Delta\epsilon^s$ are independent of z. Note that ΔT is independent of time but that $\Delta\epsilon^s$ contains the time dependence of the void-swelling law used. The quantity in the brackets of Eq. 21.79 is independent of z; so the differential equation can be integrated analytically. The solution that satisfies Eq. 21.68 is

$$v(z,t) = \frac{1}{2}\left(\frac{\alpha\,\Delta T}{2h} + \frac{\Delta\epsilon^s}{2h} \right) z^2$$
$$- \frac{[F(t) + C\Phi E \int_0^t F(t')\, dt']}{2EI}\left(L - \frac{z}{3} \right) z^2 \qquad (21.80)$$

The nature of the mechanical loading of the assembly must be specified before the force $F(t)$ can be determined. We suppose that the force F is that required to pin the top of the assembly in its original position so that

$$v(L) = 0 \qquad (21.81)$$

Therefore the right-hand side of Eq. 21.80 is set equal to zero at $z = L$, and the following integral equation for $F(t)$ results:

$$F(t) + C\Phi E \int_0^t F(t')\, dt' = \frac{3EI}{4hL}(\alpha\,\Delta T + \Delta\epsilon^s) \qquad (21.82)$$

where the second term on the left-hand side represents the effects of creep. At $t = 0$, this term and the void-swelling contribution in the second term on the right-hand side both vanish, and the required restraining force is

$$F(0) = \frac{3EI}{4hL}\alpha\,\Delta T \qquad (21.83)$$

To solve the integral equation for $F(t)$, we take the derivative of Eq. 21.82 with respect to time, noting that $\alpha\,\Delta T$ is constant in time

$$\frac{dF}{dt} + C\Phi E\, F(t) = \frac{3EI}{4hL}\Delta\dot\epsilon^s \qquad (21.84)$$

where $\Delta\dot\epsilon^s$ is the difference in the swelling rates on either side of the wrapper tube. Solution of this first-order differential equation for $F(t)$ leads to

$$F(t) = F(0)\, e^{-C\Phi Et} + \frac{3EI}{4hL} e^{-C\Phi Et}\int_0^t e^{C\Phi Et'}\Delta\dot\epsilon^s\, dt'$$

Or, using Eq. 21.83 for $F(0)$ and integrating the last term by parts,

$$F(t) = \frac{3EI}{4hL}\left(\alpha\,\Delta T\, e^{-C\Phi Et} + \Delta\epsilon^s \right)$$
$$- \frac{C\Phi E^2 I}{4hL} e^{-C\Phi Et}\int_0^t e^{C\Phi Et'}\Delta\epsilon^s\, dt' \qquad (21.85)$$

The exponential multiplying $\alpha \Delta T$ in the first term on the right represents creep relaxation of the thermal stresses. The entire second term on the right results from creep relaxation of the stresses induced by nonuniform swelling across the duct.

The restraining force explicitly determined by Eq. 21.85 can be substituted into Eq. 21.80 to determine the complete time- and position-dependent deflection of the assembly. When the core restraint is removed and the power is shut off, the terms $F(t)$ and $\alpha \Delta T$ in the deflection equation vanish, and the unrestrained deflection is

$$v^*(z,t) = \frac{\Delta \epsilon^s}{4h} z^2 - \frac{C\Phi E}{2EI} \left(L - \frac{z_i}{3}\right) z^2 \int_0^t F(t')\, dt' \quad (21.86)$$

which includes the permanent set due to swelling (the first term on the right) and creep relaxation of the thermal and swelling strains (second term on the right). Note that creep reduces the extent of deflection in the unrestrained, cold core.

Figure 21.25 shows the results of deflection calculations using the CRASIB code.[19] The assembly deflection is forced to be zero at two upper axial locations that represent the action of core clamps at each of these elevations. Interaction between adjacent assemblies (except at the spacer pads) is not considered. Figure 21.25(a) (top) shows the thermal bowing of the restrained core. At shutdown all thermal bowing is removed. Deflection due to swelling is shown in Fig. 21.25(b). A permanent bow remains at shutdown and unclamping. The sum of the deflections in (a) and (b) yields those shown in Fig. 21.25(c). The top curve in (c) represents addition of the free bowing curve of Fig. 21.24 and the deflections due to mechanical loading at elevations shown by the arrows.
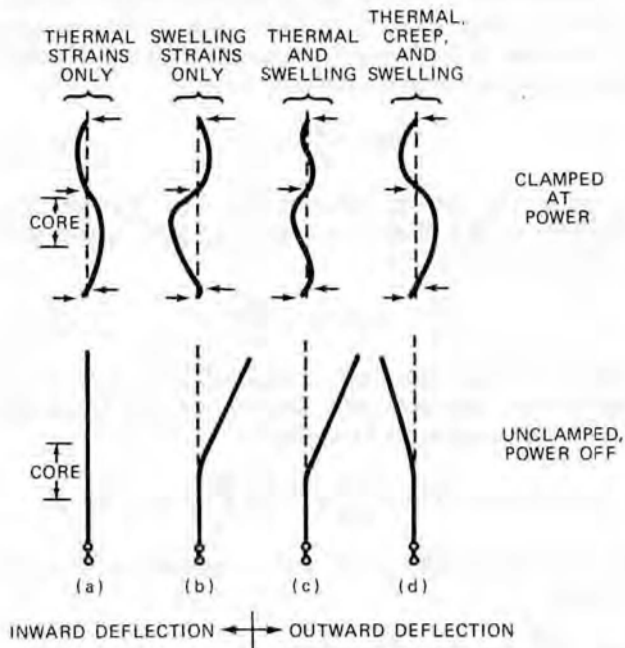
Of particular note is the sharp curvature of the "clamped at power" duct in (c), which produces large bending stresses in the duct wall. These high-stress points are effectively relaxed by irradiation creep, as shown in Fig. 21.25(d). The dramatic effect of creep on bowing is shown in the "unclamped, power off" deflections represented in (c) and (d). When creep is neglected, the duct is predicted to bow outward, whereas inclusion of irradiation creep in the calculation produces a cold unrestrained inward bow. A similar reversal of bowing direction in the fueled region of the core appears when irradiation creep is included in the analysis. At-power bowing in the core is equivalent to core expansion (outward deflection) or compaction (inward deflection) and therefore is important in estimating the neutronic reactivity of the reactor. The magnitude of the deflections of assemblies is highly sensitive to the irradiation creep law used in the bowing analysis.

21.7 SOLUTIONS TO THE SWELLING PROBLEM

It is clear from the analyses presented in this chapter that the effects of void swelling in the fuel assemblies of an LMFBR are likely to be more difficult to cope with than the design of a sturdy fuel element. Huebotter et al.[16] have reviewed a number of methods of alleviating the metal-swelling problem. Wherever possible they have estimated the increased cost of electricity generated by LMFBRs attributable to the proposed modification. These estimates should be compared with the present ~15 mills/kWh cost of nuclear power.

21.7.1 Mechanical

Two methods of accommodating swelling which form a part of the mechanical design of the core were discussed in the preceding section.

The interassembly gap must be large enough to allow for duct swelling without gross radial expansion of the core. The reduced breeding ratio and specific power that are unavoidable consequences of the lower fuel-to-metal ratio in the core will probably result in increased electric power costs as large as 0.1 mill/kWh. The larger reactor size will increase capital costs of LMFBRs, but the incremental cost has not been estimated.

Core restraint is needed to prevent extensive and possibly damaging mechanical interaction between assemblies. At least two in-core contacts, located at the spacer-pad elevations shown in Fig. 21.16, will be used. Accurate analytical prediction of the bowing of the fuel assemblies in a restrained-core design is imperative. If, as in the top drawing of Fig. 21.25(c), the deflections in the fueled zone are inward, the reactivity addition which this movement engenders must be accurately known for safety reasons. The prominent effect of irradiation creep on the magnitude and even the direction of in-core bowing implies that this form of creep needs to be thoroughly understood.

21.7.2 Neutronic

Inasmuch as swelling increases with fluence, an obvious method of reducing the swelling is to lower the maximum

THERMAL   SWELLING   THERMAL   THERMAL,
STRAINS   STRAINS   AND   CREEP,
ONLY   ONLY   SWELLING   AND SWELLING

CLAMPED AT POWER

CORE

UNCLAMPED, POWER OFF

CORE

(a)   (b)   (c)   (d)

INWARD DEFLECTION ← | → OUTWARD DEFLECTION

Fig. 21.25 Bowing of fuel assemblies with core clamps fixing the wrappers at the spacer-pad elevations. (After Ref. 18.)

burnup of the fuel. The burnup β and fluence Φt are related by Eq. 10.5:

$$\beta = q_0 \sigma_f \Phi t$$

where q_0 is the initial enrichment of the fuel in plutonium and σ_f is the fission cross section. Metal swelling varies as $(\Phi t)^n$ where $n > 1$; so appreciable reduction in void formation can be achieved by discharging fuel at reduced burnup. However, if the burnup is decreased from the target value of 10% to 5%, the fuel-cycle cost is estimated to increase by about 0.3 mill/kWh. Much of this cost increase is incurred by the more frequent fuel replacement attendant on lower burnup, which increases the frequency of fabricating fuel elements.

Instead of reducing burnup, the fluence may be decreased by increasing the fuel enrichment q_0. The obvious disadvantage of this solution is the higher cost for fuel rich in plutonium.

21.7.3 Operational

Reduction of the sodium coolant temperature lowers the wrapper temperatures correspondingly and hence reduces swelling. However, the thermodynamic efficiency of the reactor plant is reduced because of the lower sodium outlet temperature. Lowering of the sodium outlet temperature from 600°C to 500°C increases the cost of electricity by about 0.3 mill/kWh, but this cost is offset by higher plant availability when the system is operated at a lower temperature level.

Periodic rotation of assemblies by 180° is a method of smoothing out nonuniform swelling that leads to bowing. Alternatively, assemblies may be removed from the core occasionally and straightened by annealing at temperatures high enough to eliminate voids from the metal (about 800°C). The former method reduces plant availability, and the latter requires a higher fuel inventory on site, both of which carry with them undesirable economic consequences.

21.7.4 Metallurgical

Maximum stainless-steel swelling occurs within the design temperature range of the sodium coolant in the core. Use of a refractory metal with a swelling temperature range above that of the sodium in the LMFBR would alleviate the swelling problem. Replacement of stainless steel in the entire core (or at least such components as the wrapper tubes in the high flux zones) by molybdenum, for example, would permit elimination of abnormally large interassembly gaps and obviate the need for core clamps. Even with these savings, the energy cost from LMFBRs with all-molybdenum cores would be ∼0.1 mill/kWh higher than the cost of power from conventional designs. Molybdenum is more difficult to fabricate and has a higher absorption cross section for fast neutrons than does stainless steel.

The most desirable metallurgical solution to the swelling problem appears to be the modification of commercial alloys. We have seen that each of the various alloys has individual properties that are uniquely suited to fast reactor service; Nimonic PE16 is quite resistant to swelling because its microstructure contains finely divided precipitate particles that act as recombination centers for vacancies and interstitials; titanium additions reduce the susceptibility of conventional stainless steels to helium embrittlement; types 321 and 347 stainless steels do not decarburize in sodium to the same extent as do types 316 and 304. If, by suitable metallurgical modification, a modest-cost alloy could be developed which would be more resistant to swelling than the present LMFBR core material (20% cold-worked type 316 stainless steel) yet retain the characteristic high-temperature strength and generally acceptable corrosion resistance to fuel and sodium of this alloy, the economic penalty of metal swelling would be substantially reduced.

The savings that could be realized by reducing swelling [i.e., $(\Delta V/V)_{voids}$] from 15% to 5% is estimated to be between 1 and 5 billion dollars for all LMFBRs constructed up to the year 2020. The incentive for seeking solutions to the void swelling problem is great.

21.8 NOMENCLATURE

b = beam thickness in the y-direction
C = constant in irradiation-creep formula
C_1, C_2 = constants of integration of displacement differential equation
d = grain size
E = Young's modulus
E_d, E_d' = activation energies for creep
F = axial friction force at fuel-cladding interface; force on beam
h = beam thickness in the x-direction
I = moment of inertia of a beam
k = Boltzmann's constant
$\bar{k}$ = average thermal conductivity of fuel
L = height of axial zone in fuel; length of beam
M = bending moment of beam
M_c, M_f = number of radial zones in cladding and fuel, respectively
N = number of axial zones; number of cracks in a region
p_c = coolant pressure
p_{fc} = fuel—cladding interfacial pressure
p_p = plenum pressure
$\mathscr{P}$ = linear power
P_0 = porosity of as-fabricated fuel
r = radial position in fuel element
r_{ai} = inner radial boundary of zone i
r_{bi} = outer radial boundary of zone i
r_0 = radius of central void
R = fuel radius
R_c = radius of uncracked portion of fuel
t = time
t_c = cladding thickness
t_{gap} = gap thickness
t_{gap}^o = gap thickness in as-fabricated fuel element
T = temperature
T_c = temperature at root of crack in fuel; cladding temperature
T_0 = fuel center-line temperature
T_s = fuel surface temperature

u = radial displacement
v = deflection of beam
v* = unrestrained deflection
$\Delta V/V$ = swelling
x = direction along beam axis in the plane of bending
y = direction along beam axis perpendicular to the plane of bending
z = distance along the long axis of beam

Greek Letters

α = linear coefficient of thermal expansion
ϵ_i = strain component in principal direction i
ϵ^* = equivalent strain
$\dot{\epsilon}$ = creep rate
θ = angle
μ_{sf} = coefficient of static friction
μ_{sl} = coefficient of sliding friction
ν = Poisson's ratio
ρ = radius of curvature of a bent beam
σ_i = stress component in principal direction i
σ^* = equivalent stress
σ_0 = initial stress
Φ = fast neutron flux

Subscripts and Superscripts

c = creep/plastic deformation; cladding
f = fuel
h = hydrostatic
i = radial position of zone in fuel pin
j = axial position of zone in fuel pin
r = radial
s = swelling
z = axial
θ = tangential
' = values of fuel mechanical properties changed by cracking

21.9 REFERENCES

1. V. Z. Jankus and R. W. Weeks, LIFE-I: A Fortran-IV Computer Code for the Prediction of Fast Reactor Fuel-Element Behavior, USAEC Report ANL-7736, Argonne National Laboratory, 1970.
2. V. Z. Jankus and R. W. Weeks, *Nucl. Eng. Des.*, 18: 83 (1972).
3. R. Godesar, M. Guyette, and N. Hoppe, *Nucl. Appl. Technol.*, 9: 205 (1970).
4. M. Guyette, *Nucl. Eng. Des.*, 18: 53 (1972).
5. C. M. Friedrich and W. H. Guilinger, CYRGO-2: A Fortran-IV Computer Program for Stress Analysis of the Growth of Cylindrical Fuel Elements with Fission-Gas Bubbles, USAEC Report WAPD-TM-547, Bettis Atomic Power Laboratory, 1966.
6. E. Duncombe, C. M. Friedrich, and W. H. Guilinger, *Nucl. Technol.*, 12: 194 (1970).
7. S. Oldberg, Jr., BEHAVE-2: Oxide Fuel Performance Code in Two Spatial Dimensions and Time, USAEC Report GEAP-13788, General Electric Company, 1972.
8. F. J. Homan, W. J. Lackey, and C. M. Cox, FMODEL: A Fortran-IV Computer Code to Predict In-Reactor Behavior of LMFBR Fuel Pins, USAEC Report ORNL-4825, Oak Ridge National Laboratory, 1973.
9. J. R. Matthews, *Advan. Nucl. Sci. Technol.*, 6: 66 (1972).
10. E. Duncombe and I. Goldberg, *Nucl. Appl. Technol.*, 9: 47 (1970).
11. J. T. A. Roberts and B. J. Wrona, *J. Amer. Ceram. Soc.*, 56: 297 (1973).
12. J. B. Ainscough and F. Rigby, *J. Nucl. Mater.*, 47: 245 (1973).
13. Aas Steiner, *Nucl. Eng. Des.*, 21: 237 (1972).
14. J. D. Stephen, R. E. Murata, S. Vaidyanathan, J. E. Turner, and W. G. Meinhardt, LIFE-II Fuel Performance Code: Evaluation of Predictions of Cladding Inelastic Strain, USAEC Report GEAP-13951-1, General Electric Company, 1973.
15. D. P. Hines, S. Oldberg, and E. L. Zebroski, *Nucl. Appl. Technol.*, 9: 338 (1970).
16. P. R. Huebotter, T. R. Bump, W. T. Sha, D. T. Eggen, and P. J. Tulford, Design, Research, and Development Implications of Metal Swelling in Fast Reactors, USAEC Report ANL-7786, Argonne National Laboratory, 1971.
17. P. R. Huebotter and T. R. Bump, Implications of Metal Swelling in Fast Reactor Design, in *Radiation-Induced Voids in Metals*, Albany, N. Y., June 9, 1971, AEC Symposium Series, No. 26 (CONF-710601), pp. 84-124, J. W. Corbett and L. C. Ianniello (Eds.), 1972.
18. P. R. Huebotter, *Reactor Technol.*, 15: 156 (1972).
19. W. H. Sutherland and V. B. Watwood, Jr., Creep Analysis of Statistically Indeterminate Beams, USAEC Report BNWL-1362, Battelle—Northwest, 1970.
20. W. H. Sutherland, *Nucl. Eng. Des.*, 11: 269 (1970).
21. D. A. Kurcera and D. Mohr, Report ANL/EBR-014, Argonne National Laboratory, 1970.

21.10 PROBLEMS

21.1

(a) Starting with Eqs. 21.23 to 21.25 and 21.27, derive the thermal-stress distribution in a solid fuel element of radius R. Neglect swelling, creep, and cracking. Assume the fuel stack is unrestrained axially. Express the tangential stress, σ_θ, by Eq. 21.49.

(b) Derive the analog of Eq. 21.49 for fully restructured fuel with the same linear power. Assume that the initial density of the fuel was 85% and that the density after restructuring is 97% throughout the fuel.

(c) Apply the tangential-stress distributions determined in (a) and (b) to a fuel pin with a linear power of 500 W/cm. Plot the distributions and indicate the radial positions where the fracture stress is reached and where the brittle—ductile transition occurs.

21.2

(a) Using the same methods as in problem 21.1, show that the maximum tangential stress in a thin-walled cladding is given by

$$(\sigma_\theta)_{max} = \frac{\alpha E}{2(1-\nu)}\Delta T_c$$

where ΔT_c is the temperature drop across the cladding.

(b) Calculate the linear power $\mathscr{P}$ at which $(\sigma_\theta)_{max}$ is equal to the yield stress of stainless steel. Use the following properties applicable to type 316 stainless steel at 1000°K:

$E = 1.4 \times 10^8$ kN/m^2
$\nu = 0.32$
$\alpha = 1.2 \times 10^{-5}$ °K^{-1}
$\sigma_Y = 2.1 \times 10^5$ kN/m^2
$k = 0.24$ W cm^{-1} °C^{-1}
$R = 0.32$ cm
$t_c = 0.038$ cm

(c) What is the equivalent plenum pressure that would give the same maximum tangential stress as calculated in **(b)** if the cladding were isothermal? (See problem 18.6.)

(d) For a linear power one-half that determined in **(b)**, calculate the expected lifetime of the fuel cladding. Use an appropriate plot of rupture time from Chap. 18 in the calculation.

(e) If the cladding is simultaneously subject to linear power $\mathscr{P}$ and a plenum pressure p_p, what is the optimum cladding thickness based on thermoelasticity theory?

21.3 Consider a long thin-walled cylinder of inside radius R and wall thickness t_c. The tube is closed at both ends and contains a gas at pressure p_p. The system is isothermal. Assume that the tube deforms with a creep law

$$\dot{\epsilon}^* = B(\sigma^*)^n$$

Using the stress components appropriate to the thin-walled-tube situation, determine the tangential creep rate. Compare the diametral strain due to creep with that due to elastic deformation only.

21.4 At room temperature a fuel element has a fuel radius of R_0 and a fuel–cladding gap of t_{gap}^0, which is much smaller than R_0. The coefficients of thermal expansion and compressibility of the fuel material are α_f and β_f, respectively. (Note that the compressibility is the reciprocal of the bulk modulus.) The thermal-expansion coefficient of the cladding is α_c. Assume $\alpha_f > \alpha_c$. The thermal expansion coefficients are here defined on a volume (not linear) basis. The fuel element is then heated externally so that the temperature rise is everywhere uniform (no temperature gradients).

(a) At what temperature T^* does the fuel–cladding gap close? At the same time that the fuel–cladding gap closes, the top and bottom of the fuel contact the ends of the cladding; thus, at $T = T^*$ the fuel completely fills the cladding. As the temperature is increased above T^*, the fuel and cladding interact. The cladding may be assumed to be perfectly rigid and capable of thermal deformation only. The fuel is 100% dense but is completely plastic (i.e., $E = 0$ and $\nu = \frac{1}{2}$).†

(b) From thermodynamic considerations, what pressure is generated in the fuel element at $T > T^*$?

21.5 A long solid cylindrical fuel element is heated uniformly (no temperature gradients) and contacts a totally

---

†Even though $E = 0$ and $\nu = \frac{1}{2}$, the bulk modulus, which is equal to $E/3\,(1 - 2\nu)$, is *not* zero.

---

rigid cladding at a temperature T^*. For $T > T^*$ the expanding fuel is subjected to interfacial pressure p_{fc} from the cladding. The cladding is not permitted to expand either elastically or thermally; so the displacement of the outer radius of the fuel is always zero. Calculate the interfacial pressure for $T > T^*$, assuming that the fuel responds thermoelastically and in plane strain. Neglect creep. Consider two limiting cases:

1. Complete axial restraint of the fuel ($\epsilon_z = 0$). Compare this result with that obtained in problem 21.4(b).

2. No axial restraint on the fuel. Assume that the fuel is free to slip axially relative to the rigid cladding.

21.6 A sphere of fuel (denoted by "1") of radius R is embedded in an infinite medium (denoted by "2"). The two materials are in contact with no stresses at temperature zero. In a neutron flux the fuel generates heat at a uniform volumetric rate H, and the fuel radius is R.

(a) What is the temperature distribution in each material? (Assume the fuel–cladding-gap resistance is negligible whether the gap is open or closed.)

(b) Derive the thermoelasticity equation for the radial stress distribution and solve the differential equations in both regions. Using appropriate boundary conditions, solve for the complete radial stress distribution. What is the criterion for the gap to be open? If the gap is closed, express the solution in terms of the interfacial pressure p_{fc}.

(c) For the closed-gap case, determine the interfacial pressure p_{fc}.

21.7

(a) Calculate the average axial temperature distribution in the cladding in a subassembly for the following conditions:

Sodium inlet temperature, 470°C
Sodium outlet temperature, 650°C
Sodium heat-transfer coefficient, 12 W/cm^{-2} °C^{-1}
Cladding thermal conductivity, 0.22 W/cm^{-1} °C^{-1}
Cladding thickness, 0.038 cm
Linear power, 550 cos $(\pi z/2L)$, W/cm

(b) Calculate the axial fast flux profile assuming that the fuel contains 15% plutonium and has an average fission cross section of 2 barns.

(c) Calculate the void swelling profiles in the cladding using the empirical equation given in Chap. 19 for 20% cold-worked type 316 stainless steel.

21.8 Consider two adjacent fuel subassembly ducts with a clearance of δ between them. The ducts have temperature gradients across them of ∇T_1 and ∇T_2, respectively, where $\nabla T_1 > \nabla T_2$. They are supported at the grid plate in cantilever fashion [i.e., $v(0) = v'(0) = 0$]. The length of the ducts is L, and their moment of inertia is I.

(a) What values of the difference $(\nabla T_1 - \nabla T_2)$ cause the two ducts to just make contact at the top when the temperature gradients are applied?

(b) If the condition in (a) is exceeded, what are the deflections $v_1(x)$ and $v_2(x)$? What is the magnitude of the interaction force F between the two assemblies at the top? Neglect swelling and creep.

21.9   A beam cantilevered at the bottom is restrained by a spring at height L. The restoring force exerted by the spring on the beam is proportional to the deflection at z = L. The spring constant is k. (See sketch.)

   (a) Determine the deflection $v(z,t)$ when the beam is subject to an axially uniform temperature difference ΔT between opposite sides. Neglect swelling but include irradiation creep ($\dot{\epsilon} = C\sigma\Phi$).

   (b) What is the permanent deflection of the beam when the temperature difference, the neutron flux, and the spring loading are removed?
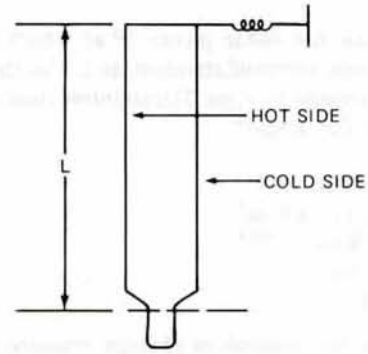
Appendix—Elasticity Theory

A.1 EQUILIBRIUM CONDITIONS

Figure A.1 shows an interior region of a solid bounded by the closed surface S. If the region contained in S is not accelerating, Newton's law of motion requires that the components of the forces on the region in each of the coordinate directions must be zero. If body forces such as gravity are neglected, the only forces acting on the region are those exerted on the surface S by the material outside S.
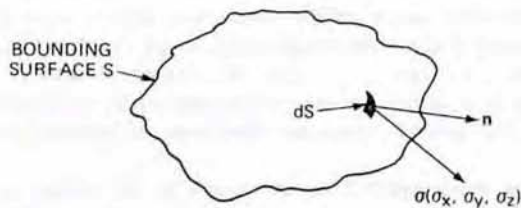

BOUNDING SURFACE S

dS

n

$\sigma(\sigma_x, \sigma_y, \sigma_z)$

Fig. A.1   Region in a solid.

The forces on the surface S can be represented by a stress vector σ, which has components σ_x, σ_y, and σ_z in the three directions of a Cartesian coordinate system. The magnitude and direction of the stress vector vary with position on the surface S. Figure A.1 shows a small element of area dS of the surface S. The outward normal to the surface at that point is denoted by n. The stress vector at the location of dS will in general have a component along the normal, which represents a normal stress, and components tangent to the surface element, which are shear stresses.

The x-component of the force on the element of surface dS is σ_x dS. The x-component of the net x force on the entire region enclosed by the surface S is the surface integral of σ_x dS. At equilibrium this integral and its counterparts in the y- and z-directions must be zero, or

$$\int_S \sigma_x \, dS = 0$$

$$\int_S \sigma_y \, dS = 0 \qquad (A.1)$$

$$\int_S \sigma_z \, dS = 0$$

To express σ_x, σ_y, and σ_z in a more convenient manner, we consider the surface element dS in Fig. A.1 to be the oblique face of a very small tetrahedron, as shown in Fig. A.2. The three mutually perpendicular planes of the tetrahedron are each perpendicular to one of the coordinate axes. The components of σ can be expressed in terms of the unit normal n and the three stress vectors acting on coordinate faces. The stress vectors on each coordinate plane are resolved into a normal stress component (e.g., σ_{xx}) and two shear components (e.g., σ_{xy} and σ_{xz}) that act tangentially to the coordinate plane.

The components of the stress vectors on the coordinate planes are written as σ_{ij}, where i refers to the coordinate plane in which the stress acts (e.g., σ_{xx}, σ_{xy}, and σ_{xz} all act on the plane perpendicular to the x axis) and j refers to the direction in which the stress component acts.

The area of each of the coordinate planes in Fig. A.2 is a projected area of the oblique face dS. The area over which σ_{xx}, σ_{xy}, and σ_{xz} act is n · i dS = n_x dS, where i, j, and k are the unit vectors in the x, y, and z directions, respectively. The direction cosines of the surface normal are n_x = n · i, n_y = n · j, and n_z = n · k.

The tetrahedron of Fig. A.2 is in mechanical equilibrium owing to the forces on its four faces, or the net force

z

dS

σ_{xx}

σ_{xy}

σ_{xz}

n

$\sigma(\sigma_x, \sigma_y, \sigma_z)$

σ_{yy}

σ_{yx}

σ_{yz}
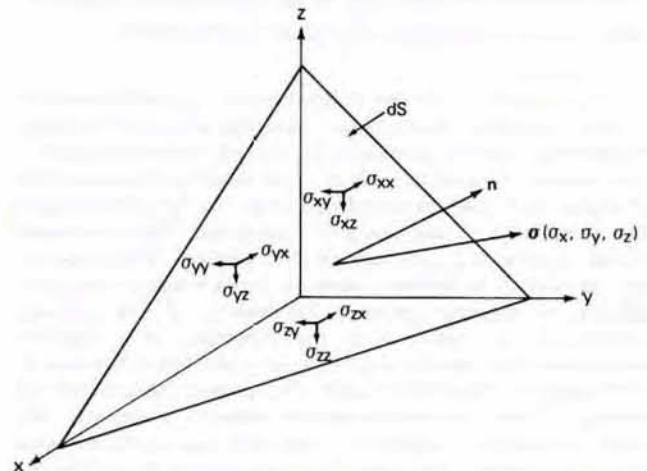
σ_{zx}

σ_{zy}

σ_{zz}

y

x

Fig. A.2   Diagram for relating surface forces to nine components of stress tensor.

in each coordinate direction is zero. According to the sign convention,* force components on the coordinate faces are positive if pointing toward the negative coordinate axis under consideration. The x-direction force balance is

$$\sigma_x \, dS - \sigma_{xx} n_x \, dS - \sigma_{yx} n_y \, dS - \sigma_{zx} n_z \, dS = 0$$

If dS is canceled and the last three terms are written as the scalar product of n and the vector whose components are σ_{xx}, σ_{yx}, and σ_{zx}, the preceding formula becomes

$$\sigma_x = n \cdot (\sigma_{xx} i + \sigma_{yx} j + \sigma_{zx} k)$$

Similarly,

$$\sigma_y = n \cdot (\sigma_{xy} i + \sigma_{yy} j + \sigma_{zy} k)$$

$$\sigma_z = n \cdot (\sigma_{xz} i + \sigma_{yz} j + \sigma_{zz} k) \qquad (A.2)$$

Equation A.2 relates the components of the stress vector σ to the unit normal describing the orientation of the surface and the nine components of the stresses acting on the three coordinate planes, usually denoted collectively as the *stress tensor*:

$$\sigma_{ij} = \begin{pmatrix} \sigma_{xx} & \sigma_{xy} & \sigma_{xz} \\ \sigma_{yx} & \sigma_{yy} & \sigma_{yz} \\ \sigma_{zx} & \sigma_{zy} & \sigma_{zz} \end{pmatrix} \qquad (A.3)$$

An important relation between the off-diagonal elements of the tensor σ_{ij} can be obtained by applying the condition that the angular acceleration of any element of volume is zero. This restriction leads to the relations

$$\sigma_{xy} = \sigma_{yx}$$

$$\sigma_{xz} = \sigma_{zx} \qquad (A.4)$$

$$\sigma_{zy} = \sigma_{yz}$$

Or, of the nine components of the stress tensor of Eq. A.3, only six are independent; the tensor is symmetric.

---

*The signs of the stress component σ_{ij} are determined by the following convention: consider a volume element bounded by planes perpendicular to the coordinate axes. If the outward normal of one of these plane surfaces is in the direction of a positive coordinate axis, the σ_{ij} are positive if the stress acts in the positive j direction. Thus a normal stress, such as σ_{xx}, is positive if in tension. Pressures that act inward in a volume element (compression) are considered as negative stresses. Conversely, if the outward normal of the plane is in the direction of a negative coordinate axis, the σ_{ij} are positive when the stress acts in the negative j direction. Again, the normal components are positive if they place the volume element in tension. The three coordinate planes of Fig. A.2 are surfaces with negative normals, and the σ_{ij} are positive as drawn on the figure. In a force balance on the element of Fig. A.2, therefore, the contribution to the total force in the positive x-direction due to the coordinate plane perpendicular to the x axis is $-\sigma_{xx}$ times the area of the plane.

Substitution of Eq. A.2 into Eq. A.1 yields equilibrium relations in terms of the stress tensor σ_{ij}. For the x-direction, the result is

$$\int_S n \cdot (\sigma_{xx} i + \sigma_{yx} j + \sigma_{zx} k) \, dS = 0$$

Applying the divergence theorem* to the surface integral in this equation yields the final form of the equilibrium relation:

$$\frac{\partial \sigma_{xx}}{\partial x} + \frac{\partial \sigma_{yx}}{\partial y} + \frac{\partial \sigma_{zx}}{\partial z} = 0 \qquad (A.5)$$

Similarly, for the y- and z-directions, the equilibrium conditions are

$$\frac{\partial \sigma_{xy}}{\partial x} + \frac{\partial \sigma_{yy}}{\partial y} + \frac{\partial \sigma_{zy}}{\partial z} = 0 \qquad (A.6)$$

$$\frac{\partial \sigma_{xz}}{\partial x} + \frac{\partial \sigma_{yz}}{\partial y} + \frac{\partial \sigma_{zz}}{\partial z} = 0 \qquad (A.7)$$

A.2 DISPLACEMENTS

A body subjected to stress will become distorted or strained as a result. The state of strain is described by the displacement vector, which connects a point (x,y,z) in the unstrained body with the location to which this point has moved (x + u, y + v, z + w) in the strained condition. The lengths u, v, and w are the components of the displacement vector; in general, they are functions of position in the solid.

The stress applied to the body is not related to the absolute values of the displacement components. The fact that a body is made to undergo translation or rotation because of an applied force, for example, has nothing to do with the material properties of the solid. The property that is uniquely determined by the applied stress is the relative displacement of points in the solid. The solid-line rectangle in Fig. A.3 represents a plane rectangular element of dimensions δx and δy in an unstressed body (for simplicity, only two dimensions are considered). After stress has been applied, the rectangle is distorted into the dashed four-sided figure. The arrows connecting the corners of the unstrained and strained figures are the displacement vectors for these four points. The displacement vector of the point (x,y) in the lower left-hand corner has components u and v. Since the relative motion of adjacent points is small, the displacement components at other locations can be approximated by Taylor series expansions about the values at the point (x,y). Thus, the displacement components of the

---

*For a vector F defined over a region of volume V and surface S, the divergence theorem is

$$\int_S n \cdot F \, dS = \int_V \nabla \cdot F \, dV$$

where, for Cartesian coordinates,

$$\nabla \cdot F = \frac{\partial F_x}{\partial x} + \frac{\partial F_y}{\partial y} + \frac{\partial F_z}{\partial z}$$

Thus the tensor ω_{ij} of Eq. A.11 represents pure rotation of the body.

Only the deformation tensor ϵ_{ij} is determined by the stress tensor and material properties. Hooke's law is an example of such a relation for elastic deformations.

A.3 COMPATIBILITY RELATIONS

Additional relationships between the deformation components ϵ_{ij} reflect the requirement that the medium be a continuum, or that the solid has not been cracked and that there are no discontinuities in the displacements. Mathematically, these *compatibility conditions* require that certain rather obvious relations among the components of the deformation tensor exist. For example, if ϵ_{xx} is differentiated twice with respect to y, the result is $(\partial^3 u)/(\partial x\, \partial y^2)$. Similarly, if ϵ_{yy} is differentiated twice with respect to x, we obtain $(\partial^3 v)/(\partial y\, \partial x^2)$. Now if ϵ_{xy} is differentiated with respect to x and y, the result is $(1/2)[(\partial^3 u)/(\partial x\, \partial y^2) + (\partial^2 v)/(\partial x^2\, \partial y)]$, which is one-half the sum of $\partial^2 \epsilon_{xx}/\partial y^2$ and $\partial^2 \epsilon_{yy}/\partial x^2$. In all, there are six compatibility equations relating the various components of ϵ_{ij}. In Cartesian coordinates they are

$$\frac{\partial^2 \epsilon_{xy}}{\partial x\, \partial y} = \frac{1}{2}\left(\frac{\partial^2 \epsilon_{xx}}{\partial y^2} + \frac{\partial^2 \epsilon_{yy}}{\partial x^2}\right)$$

$$\frac{\partial^2 \epsilon_{xx}}{\partial y\, \partial z} = \frac{\partial}{\partial x}\left(-\frac{\partial \epsilon_{yz}}{\partial x} + \frac{\partial \epsilon_{xz}}{\partial y} + \frac{\partial \epsilon_{xy}}{\partial z}\right)$$

$$\frac{\partial^2 \epsilon_{xz}}{\partial x\, \partial z} = \frac{1}{2}\left(\frac{\partial^2 \epsilon_{xx}}{\partial z^2} + \frac{\partial^2 \epsilon_{zz}}{\partial x^2}\right)$$

$$\frac{\partial^2 \epsilon_{yy}}{\partial x\, \partial z} = \frac{\partial}{\partial y}\left(-\frac{\partial \epsilon_{xz}}{\partial y} + \frac{\partial \epsilon_{xy}}{\partial z} + \frac{\partial \epsilon_{yz}}{\partial x}\right)$$

$$\frac{\partial^2 \epsilon_{yz}}{\partial y\, \partial z} = \frac{1}{2}\left(\frac{\partial^2 \epsilon_{yy}}{\partial z^2} + \frac{\partial^2 \epsilon_{zz}}{\partial y^2}\right)$$

$$\frac{\partial^2 \epsilon_{zz}}{\partial x\, \partial y} = \frac{\partial}{\partial z}\left(-\frac{\partial \epsilon_{xy}}{\partial z} + \frac{\partial \epsilon_{yz}}{\partial x} + \frac{\partial \epsilon_{xz}}{\partial y}\right) \quad \text{(A.12)}$$

A.4 STRESS–STRAIN RELATIONS

In the absence of plastic deformation, creep, or temperature changes, the stress–strain relation is given by the generalized form of Hooke's law. For the elastic solid, the six components of the stress tensor are related to the six components of the deformation tensor by the linear equations:

$$\sigma_{xx} = c_{11}\epsilon_{xx} + c_{12}\epsilon_{yy} + c_{13}\epsilon_{zz} + c_{14}\epsilon_{yz}$$
$$+ c_{15}\epsilon_{zx} + c_{16}\epsilon_{xy}$$

$$\sigma_{yy} = c_{21}\epsilon_{xx} + c_{22}\epsilon_{yy} + c_{23}\epsilon_{zz} + c_{24}\epsilon_{yz}$$
$$+ c_{25}\epsilon_{zx} + c_{26}\epsilon_{xy}$$

$$\sigma_{zz} = c_{31}\epsilon_{xx} + c_{32}\epsilon_{yy} + c_{33}\epsilon_{zz} + c_{34}\epsilon_{yz}$$
$$+ c_{35}\epsilon_{zx} + c_{36}\epsilon_{xy}$$

$$\sigma_{yz} = c_{41}\epsilon_{xx} + c_{42}\epsilon_{yy} + c_{43}\epsilon_{zz} + c_{44}\epsilon_{yz}$$
$$+ c_{45}\epsilon_{zx} + c_{46}\epsilon_{xy}$$

$$\sigma_{zx} = c_{51}\epsilon_{xx} + c_{52}\epsilon_{yy} + c_{53}\epsilon_{zz} + c_{54}\epsilon_{yz}$$
$$+ c_{55}\epsilon_{zx} + c_{56}\epsilon_{xy}$$

$$\sigma_{xy} = c_{61}\epsilon_{xx} + c_{62}\epsilon_{yy} + c_{63}\epsilon_{zz} + c_{64}\epsilon_{yz}$$
$$+ c_{65}\epsilon_{zx} + c_{66}\epsilon_{xy} \quad \text{(A.13)}$$

The c_{ij} values are the *elastic moduli* of the medium. Not all 36 of the coefficients in Eq. A.13 are independent. Because the tensors σ_{ij} and ϵ_{ij} are symmetric, $c_{ij} = c_{ji}$, which reduces the number of elastic constants to 21. This number is reduced still further according to the symmetry of the crystal structure of the solid; the greater the symmetry, the fewer the constants. For crystals of the cubic system, there are only three elastic constants. Finally, for materials that are macroscopically isotropic (either because the substance is noncrystalline or because the material is in polycrystalline form), only two constants remain. These two elastic constants are called *Lamé coefficients* λ and μ. They determine the stress–strain relation by

$$\sigma_{ii} = 2\mu\epsilon_{ii} + \lambda\delta \quad \text{(A.14)}$$

and

$$\sigma_{ij} = 2\mu\epsilon_{ij} \quad (i \neq j) \quad \text{(A.15)}$$

Here δ is the volume dilatation, or the fractional change in volume:

$$\delta = \epsilon_{xx} + \epsilon_{yy} + \epsilon_{zz} \quad \text{(A.16)}$$

The elastic constants are usually expressed in terms of Young's modulus E, the shear modulus G, and Poisson's ratio ν, instead of the Lamé coefficients. The relations between the conventional elastic moduli and the Lamé coefficients are

$$E = \frac{\mu(3\lambda + 2\mu)}{\lambda + \mu} \quad \text{(A.17)}$$

$$G = \mu \quad \text{(A.18)}$$

$$\nu = \frac{\lambda}{2(\lambda + \mu)} \quad \text{(A.19)}$$

The values E, G, and ν are not independent but are related by

$$G = \frac{E}{2(1 + \nu)} \quad \text{(A.20)}$$

Using Eqs. A.17 to A.19 in Eqs. A.14 and A.15 and solving for the strains yields

$$\epsilon_{xx} = \frac{1}{E} [\sigma_{xx} - \nu(\sigma_{yy} + \sigma_{zz})]$$

$$\epsilon_{yy} = \frac{1}{E} [\sigma_{yy} - \nu(\sigma_{xx} + \sigma_{zz})] \quad (A.21)$$

$$\epsilon_{zz} = \frac{1}{E} [\sigma_{zz} - \nu(\sigma_{xx} + \sigma_{yy})]$$

$$\epsilon_{xy} = \frac{1}{2G}\sigma_{xy} \quad \epsilon_{xz} = \frac{1}{2G}\sigma_{xz} \quad \epsilon_{yz} = \frac{1}{2G}\sigma_{yz} \quad (A.22)$$

In addition to the elongations caused by applied stresses, a change in temperature produces normal strains (but not shear strains) given by

$$(\epsilon_{ii})_{thermal} = \alpha\,\Delta T \quad (A.23)$$

where α is the coefficient of linear thermal expansion and ΔT is the temperature rise with respect to a reference temperature. The thermal component given by Eq. A.23 is added to each of the normal strains given by Eq. A.21 to produce the total strain.

Effects other than applied stress or temperature change can contribute to the strain. In analyses of the performance of reactor fuel elements, for example, the elongations of Eq. A.21 are supplemented by contributions due to creep and fission-product swelling. Like the thermal component of the strain, these effects are accommodated into the stress–strain relations by adding appropriate terms to the right-hand sides of Eq. A.21. Relations such as Eqs. A.21 and A.22 to which other sources of displacement have been appended are known as *constitutive relations*.

A.5 ELASTIC STRAIN ENERGY

The strain of a solid as a result of applied stresses means that work has been done on the material. This work is stored as internal energy, or *elastic strain energy*, in the medium.

The strain energy can best be illustrated by considering the one-dimensional analog of the solid, namely, the elastic string. If sufficient force is applied to a string to extend its length from x_0 to x_f, the work done in the process is

$$W = k \int_{x_0}^{x_f} (x - x_0)dx = \frac{1}{2}k(x_f - x_0)^2$$

Here k is the Hooke's law constant of the string. The force on the string in the final state is

$$F = k(x_F - x_0)$$

The work done can also be written as

$$W = \frac{1}{2}F(x_F - x_0)$$

The elastic energy E_{el} stored in a unit length of string is W/x_0. The strain ϵ of the string is $(x_f - x_0)/x_0$. Dividing the preceding formula by the initial length yields

$$E_{el} = \frac{1}{2}F\epsilon \quad (A.24)$$

In a three-dimensional elastic medium, the single force F is replaced by the components of the stress tensor, and the strain is represented by the deformation tensor. The strain energy per unit volume is

$$E_{el} = \frac{1}{2}(\sigma_{xx}\epsilon_{xx} + \sigma_{yy}\epsilon_{yy} + \sigma_{zz}\epsilon_{zz} + 2\sigma_{xy}\epsilon_{xy}$$
$$+ 2\sigma_{xz}\epsilon_{xz} + 2\sigma_{yz}\epsilon_{yz}) \quad (A.25)$$

The elastic-energy density can also be written in terms of the stresses alone by substituting Eq. A.21 into Eq. A.25:

$$E_{el} = \frac{1}{2E}(\sigma_{xx}^2 + \sigma_{yy}^2 + \sigma_{zz}^2) - \frac{\nu}{E}(\sigma_{xx}\sigma_{yy} + \sigma_{xx}\sigma_{zz}$$
$$+ \sigma_{yy}\sigma_{zz}) + \frac{1}{2G}(\sigma_{xy}^2 + \sigma_{xz}^2 + \sigma_{yz}^2) \quad (A.26)$$

For the case of a simple hydrostatic stress system ($\sigma_{xx} = \sigma_{yy} = \sigma_{zz} = \sigma$ and $\sigma_{xy} = \sigma_{xz} = \sigma_{yz} = 0$), Eq. A.26 reduces to

$$E_{el} = \frac{\sigma^2}{2K} \quad (A.27)$$

where

$$K = \frac{E}{3(1 - 2\nu)} \quad (A.28)$$

is the bulk modulus, which is the reciprocal of the coefficient of compressibility (see problem 1.5, Chap. 1).

A.6 CYLINDRICAL COORDINATES

The behavior of a solid under applied stresses is determined by simultaneous application of the equilibrium conditions (Sec. A.1), the compatibility conditions (Sec. A.3), and a stress–strain relation (Sec. A.4). Strains and displacements are related by the components of the deformation tensor (Sec. A.2).

The analysis up to this point has been conducted in terms of Cartesian coordinates. However, many important problems (e.g., the stresses around a dislocation or in a reactor fuel element) are more conveniently treated in cylindrical coordinates. For this purpose the four relations listed in the preceding paragraph must be transformed from rectangular to cylindrical coordinates.

Transformation of the stress–strain relation requires only the replacement of x, y, and z in Eqs. A.21 and A.22 by the radial, azimuthal, and axial coordinates r, θ, and z.

Since the number of relevant strain components is considerably reduced when simple shapes are treated, the compatibility relations for cylindrical coordinates are best determined from the set of strain components peculiar to the problem at hand. The method of generating compatibility relations for cylindrical coordinates is analogous to that used in Sec. A.3 for rectangular coordinates.

Transformation of the equilibrium relations and the components of the deformation tensor is straightforward but tedious. The results are

Equilibrium conditions:

$$\frac{1}{r}\frac{\partial}{\partial r}(r\sigma_{rr}) + \frac{1}{r}\frac{\partial\sigma_{r\theta}}{\partial\theta} - \frac{1}{r}\sigma_{\theta\theta} + \frac{\partial\sigma_{rz}}{\partial z} = 0 \quad (A.29)$$

$$\frac{1}{r}\frac{\partial\sigma_{\theta\theta}}{\partial\theta} + \frac{\partial\sigma_{r\theta}}{\partial r} + \frac{2}{r}\sigma_{r\theta} + \frac{\partial\sigma_{\theta z}}{\partial z} = 0 \quad (A.30)$$

$$\frac{1}{r}\frac{\partial}{\partial r}(r\sigma_{rz}) + \frac{1}{r}\frac{\partial\sigma_{\theta z}}{\partial\theta} + \frac{\partial\sigma_{zz}}{\partial z} = 0 \quad (A.31)$$

Components of the deformation tensor:

$$\epsilon_{rr} = \frac{\partial u_r}{\partial r} \quad \epsilon_{\theta\theta} = \frac{u_r}{r} + \frac{1}{r}\frac{\partial u_\theta}{\partial\theta} \quad \epsilon_{zz} = \frac{\partial u_z}{\partial z} \quad (A.32)$$

$$\epsilon_{r\theta} = \epsilon_{\theta r} = \frac{1}{2}\left(\frac{1}{r}\frac{\partial u_r}{\partial\theta} + \frac{\partial u_\theta}{\partial r} - \frac{u_\theta}{r}\right)$$

$$\epsilon_{rz} = \epsilon_{zr} = \frac{1}{2}\left(\frac{\partial u_r}{\partial z} + \frac{\partial u_z}{\partial r}\right) \quad (A.33)$$

$$\epsilon_{z\theta} = \epsilon_{\theta z} = \frac{1}{2}\left(\frac{\partial u_\theta}{\partial z} + \frac{1}{r}\frac{\partial u_z}{\partial\theta}\right)$$

Stress components and displacements in cylindrical coordinates are shown in Fig. A.4. The θ-direction is orthogonal to the radial and axial directions.

A.7 NOMENCLATURE

c_{ij} = coefficients of generalized Hooke's law (elastic moduli)
E = Young's modulus
E_{el} = elastic strain energy per unit volume
F = force
G = shear modulus
i,j,k = unit vectors
K = bulk modulus
n = outward normal to surface
r,θ,z = cylindrical coordinates
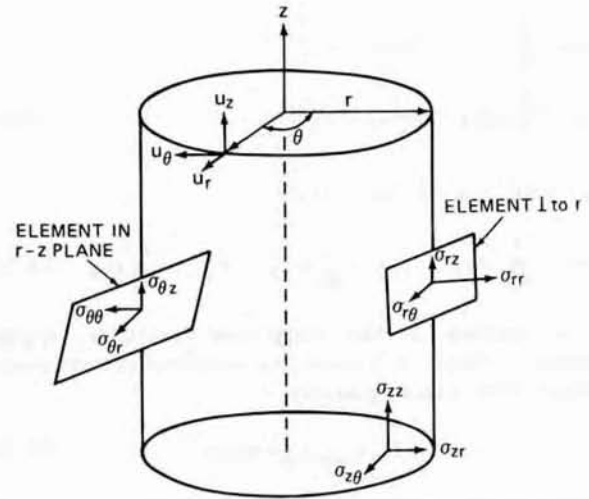

Fig. A.4 Stress components and displacements in the cylindrical coordinate system.

S_{ij} = strain tensor
T = temperature
u,v,w = components of displacement vector
W = work
x,y,z = Cartesian coordinates

Greek Letters
α = coefficient of linear thermal expansion
δ = volume dilation
ϵ_{ij} = symmetric deformation tensor (strain components)
λ,μ = Lamé constants for an isotropic solid
ν = Poisson's ratio
σ_{ij} = stress tensor (stress components)
ω_{ij} = skew-symmetric rotation tensor

A.8 ADDITIONAL READING

1. J. Weertman and J. R. Weertman, *Elementary Dislocation Theory*, Chap. 2, The Macmillan Company, New York, 1964.
2. Z. Zudans, T. C. Yen, and W. H. Steigelmann, *Thermal Stress Techniques in the Nuclear Industry*, Chap. 3, American Elsevier Publishing Company, Inc., New York, 1965.